



LONGITUDINAL PROPERTIES OF A WIDESPREAD SOLAR ENERGETIC PARTICLE EVENT ON 2014 FEBRUARY 25: EVOLUTION OF THE ASSOCIATED CME SHOCK

D. LARIO¹, R.-Y. KWON^{1,2}, A. VOURLIDAS¹, N. E. RAOUFI¹, D. K. HAGGERTY¹, G. C. HO¹, B. J. ANDERSON¹,
A. PAPAIOANNOU³, R. GÓMEZ-HERRERO⁴, N. DRESING⁵, AND P. RILEY⁶

¹The Johns Hopkins University, Applied Physics Laboratory, Laurel, MD 20723, USA

²School of Physics, Astronomy and Computational Sciences, George Mason University, 4400 University Drive, MSN 6A2, Fairfax, VA 22030, USA

³Institute for Astronomy, Astrophysics, Space Applications and Remote Sensing, National Observatory of Athens, GR-15 236 Penteli, Greece

⁴Space Research Group, Physics and Mathematics Department, University of Alcalá, Alcalá de Henares, E-28871, Spain

⁵Institute of Experimental and Applied Physics, Christian-Albrechts University of Kiel, Kiel, Germany

⁶Predictive Science, 9990 Mesa Rim Road, Suite 170, San Diego, CA 92121, USA

Received 2015 October 5; accepted 2016 January 18; published 2016 February 29

ABSTRACT

We investigate the solar phenomena associated with the origin of the solar energetic particle (SEP) event observed on 2014 February 25 by a number of spacecraft distributed in the inner heliosphere over a broad range of heliolongitudes. These include spacecraft located near Earth; the twin *Solar Terrestrial Relations Observatory* spacecraft, *STEREO-A* and *STEREO-B*, located at ~ 1 au from the Sun 153° west and 160° east of Earth, respectively; the *MERCURY SURFACE SPACE ENVIRONMENT GEOCHEMISTRY AND RANGING* mission (at 0.40 au and 31° west of Earth); and the *Juno* spacecraft (at 2.11 au and 48° east of Earth). Although the footpoints of the field lines nominally connecting the Sun with *STEREO-A*, *STEREO-B* and near-Earth spacecraft were quite distant from each other, an intense high-energy SEP event with Fe-rich prompt components was observed at these three locations. The extent of the extreme-ultraviolet wave associated with the solar eruption generating the SEP event was very limited in longitude. However, the white-light shock accompanying the associated coronal mass ejection extended over a broad range of longitudes. As the shock propagated into interplanetary space it extended over at least $\sim 190^\circ$ in longitude. The release of the SEPs observed at different longitudes occurred when the portion of the shock magnetically connected to each spacecraft was already at relatively high altitudes ($\gtrsim 2 R_\odot$ above the solar surface). The expansion of the shock in the extended corona, as opposite to near the solar surface, determined the SEP injection and SEP intensity-time profiles at different longitudes.

Key words: acceleration of particles – Sun: activity – Sun: coronal mass ejections (CMEs) – Sun: heliosphere – Sun: particle emission

1. INTRODUCTION

The combination of observations performed simultaneously by a number of spacecraft located at distant heliospheric locations is the primary tool to investigate the spatial distribution of solar energetic particle (SEP) events (e.g., McKibben 1972; McGuire et al. 1983; Kallenrode et al. 1992; Reames et al. 1996; Lario et al. 2000, 2003, 2006, 2013; McKibben et al. 2003; Wibberenz & Cane 2006; Dresing et al. 2012, 2014; Rouillard et al. 2012; Park et al. 2013; Wiedenbeck et al. 2013; Papaioannou et al. 2014; Richardson et al. 2014; Gómez-Herrero et al. 2015). The most intense SEP events, originally associated with gradual solar flares (i.e., flares with time durations of the 1–8 Å soft X-ray (SXR) emission at 0.1 of the peak intensity longer than 1 hr; cf. Cane et al. 1986), can be simultaneously observed over a wide range of heliolongitudes. For example, Kallenrode et al. (1992) showed that SEP events associated with gradual flares were observed by spacecraft whose nominal magnetic footpoints were distant from the parent solar flare site by up to $\pm 120^\circ$ in longitudinal distance. Observations carried out by single spacecraft orbiting near Earth have also shown several cases of SEP events that originated close to 180° from the central meridian line (e.g., Dodson & Hedeman 1969; Torsti et al. 1999a; Cliver et al. 2005) or from longitudes close to the east limb, and therefore poorly connected to a near-Earth observer (e.g., Cliver et al. 1995). Observations carried out by several spacecraft widely distributed in heliolongitude have allowed

the observation of SEP events filling a very broad region around the Sun (e.g., Richardson et al. 2014; Gómez-Herrero et al. 2015, and references therein).

Such widespread events have been often interpreted in terms of particle acceleration by shocks driven by coronal mass ejections (CMEs) that are able to inject SEPs over broad angular regions (e.g., Cane et al. 1988; Cliver et al. 1995; Reames et al. 1996). Processes of cross-field diffusion, where particles can effectively propagate perpendicular to the average direction of the interplanetary magnetic field (IMF), have also been suggested as important contributors to the spread of energetic particles in the heliosphere (e.g., Zhang et al. 2009; Dresing et al. 2012; Dröge et al. 2014; Strauss & Fichtner 2015). Meandering of field lines due to plasma turbulence may also help to spread SEPs in longitude (e.g., Laitinen et al. 2015b, and references therein). In order to model SEP intensities simultaneously observed by spacecraft that are well separated in longitude, a full characterization of the particle sources in the corona and interplanetary space is required. This includes specification of the spatial extent, location and time duration of the particle sources.

Whereas particle acceleration by CME-driven shocks covering or propagating over large longitudinal distances facilitates the injection of SEPs over a broad range of longitudes, it is important to emphasize that direct observational evidence of wide shocks in the corona and in interplanetary space able to inject SEPs over a wide range of longitudes is very limited. Regarding the extent of shocks in interplanetary (IP) space,

evidence shows that the width of IP shocks in the inner heliosphere is finite. For example, Richardson & Cane (1993) concluded that shock drivers (understood as the ejecta or the interplanetary counterpart of the CME, henceforth ICME) can extend at 1 au up to a full-width of about 100° in longitude, centered on the solar source longitude. The interplanetary shocks themselves extend beyond the longitudinal span of the corresponding ICME, but their longitudinal extent at 1 au is at most 180° (e.g., Cane 1996, and references therein). de Lucas et al. (2011) used in situ observations from *Helios*, *IMP-8*, and *ISEE-3* to determine the angular extent of CME-driven shocks and concluded that an IP shock has about a 50% chance of being observed at two locations separated by 90° in longitude. The fraction of shocks observed by multiple spacecraft clearly drops off for separation angles larger than 100° , and only four cases were found by de Lucas et al. (2011) for angular separations between 120° and 160° . A separate question is whether these wide shocks are able to accelerate particles when they are observed in situ by the spacecraft (e.g., Lario et al. 2005; Giacalone 2012).

Regarding the extent of shocks in the corona, there have been several attempts to relate wave-like large-scale disturbances propagating over the solar disk in extreme-ultraviolet (EUV) observations (usually referred to as EIT waves or EUV waves) with coronal shocks able to inject SEPs over a broad range of heliolongitudes (e.g., Bothmer et al. 1997; Posner et al. 1997; Krucker et al. 1999; Torsti et al. 1999b; Rouillard et al. 2012; Park et al. 2013, 2015; Lario et al. 2014; Miteva et al. 2014; Prise et al. 2014). For example, Park et al. (2013) hypothesized that EIT waves can be used to track the expansion of a coronal shock responsible for particle acceleration and injection at the footpoints of the IMF lines connecting to several spacecraft. However, other authors concluded that the propagation of the EIT wave close to the solar surface could not be used as a proxy for the expansion of the coronal source of SEPs since EIT waves are not always observed to reach the magnetic footpoints of spacecraft detecting SEPs (e.g., Posner et al. 1997; Lario et al. 2014; Prise et al. 2014). In particular, Prise et al. (2014) and Lario et al. (2014) concluded that the factor that determines the longitudinal expansion of the SEP events is the shock wave associated with the CME in the extended corona, rather than the EUV wave at the coronal base. EUV waves are thought to be the footprints of the lateral propagation of shock waves initially driven by CMEs (e.g., Patsourakos & Vourlidis 2009; Kwon et al. 2013, 2014). Whereas the front or leading edge of the CME expands away from the Sun, magnetic field structures in the low corona (such as active regions, coronal loops and/or coronal holes) may disrupt the propagation of the EUV waves by stopping, decelerating or reflecting them (e.g., Wills-Davey & Thompson 1999; Veronig et al. 2006). Therefore, the shock wave associated with the CME may continue to expand at high altitudes without leaving any EUV trace visible near the solar surface.

In 2014 February the distribution of spacecraft in the inner heliosphere allowed us to analyze an intense SEP event occurring on 2014 February 25 from multiple vantage points. This SEP event was not only observed by spacecraft located near Earth (e.g., the *Advanced Composition Explorer* (*ACE*), the *Solar and Heliospheric Observatory* (*SOHO*), the *Geostationary Operational Environmental Satellites* (*GOES*), and *Wind*), but also by the two *Solar TERrestrial RELations*

Observatory spacecraft (*STEREO-A* and *STEREO-B*) near ~ 1 au, the *MERCURY Surface, Space ENVIRONMENT, GEOchemistry, and Ranging* (*MESSENGER*) mission orbiting around Mercury (Solomon et al. 2007), and the *Juno* spacecraft en route to Jupiter (Bagenal et al. 2014). Figure 1 shows a sketch of the spacecraft locations early on 2014 February 25 and a summary of the energetic particle observations during the SEP event made by the spacecraft considered in this work. In particular, Figure 1(a) shows the longitudinal distribution of the spacecraft, as seen from the north ecliptic pole, where the red, blue and black dots indicate the locations of *STEREO-A* (*STA*), *STEREO-B* (*STB*) and spacecraft near the Sun–Earth Lagrangian point L1, respectively, all of them at heliocentric radial distances R very close to 1 au. The green and orange dots indicate the location of *Juno* at $R = 2.11$ au and *MESSENGER* at $R = 0.40$ au, respectively. The heliocentric inertial longitude of each spacecraft (Long) is listed in the figure. Nominal Parker spiral magnetic field lines connecting each spacecraft with the Sun are also plotted in Figure 1(a).

Figures 1(b)–(f) show energetic particle intensity-time profiles measured by (b) *Juno*, (c) near-Earth spacecraft (i.e., *ACE* and *SOHO*), (d) *MESSENGER*, (e) *STEREO-A*, and (f) *STEREO-B* during the SEP event on 2014 February 25 (day of year 56). Near-relativistic electron intensities at *Juno* (Figure 1(b)) were measured by the Jovian Energetic particle Detector Instrument (JEDI; Mauk et al. 2013) and at *MESSENGER* (Figure 1(d)) by the Energetic Particle Spectrometer (EPS; Andrews et al. 2007). Near-relativistic electron intensities at L1 (top panel of Figure 1(c)) were measured by the Electron Proton and Alpha Monitor (EPAM; Gold et al. 1998) on board *ACE* and the proton intensities (bottom panel of Figure 1(c)) by *ACE/EPAM* (gray trace) and by the Energetic Relativistic Nuclei and Electron Instrument (ERNE; Torsti et al. 1995) on board *SOHO* (black trace). Near-relativistic electron intensities shown in the top panels of Figures 1(e) and (f) were measured by the Solar Electron and Proton Telescope (SEPT; Müller-Mellin et al. 2008) on board the two *STEREO* spacecraft whereas the proton intensities in the bottom panel of Figures 1(e) and (f) were measured by SEPT (gray traces) and by the High-energy Telescope (HET; von Rosenvinge et al. 2008) on board *STEREO*. Both particle telescopes SEPT and HET are part of the In situ Measurements of Particles CME Transients (IMPACT) suite of instruments (Luhmann et al. 2008).

The origin of the SEP event has been associated with an intense X4.9/2B flare with 1–8 Å soft X-ray onset at 00:39 UT on 2014 February 25 occurring at the NOAA Active Region #11990 located at S12E82 (as seen from Earth) (e.g., Gopalswamy et al. 2015). The longitude of the parent flare is indicated by the purple line labelled E82 in Figure 1(a). The purple arrows in Figures 1(b)–(f) indicate the onset time of the SXR flare emission. Significant energetic particle intensity enhancements were observed by all the selected spacecraft shortly after the occurrence of the flare regardless of their magnetic connection with the Sun. An EUV wave was observed in association with the solar flare but it did not propagate equally in all directions across the Sun (Long et al. 2015). As seen from Earth, the propagation of the EUV wave was constrained to a limited range of longitudes primarily north and south along the eastern solar limb (see details in Long et al. 2015). The Large Angle and Spectrometric Coronagraph (LASCO) on board *SOHO* (Brueckner

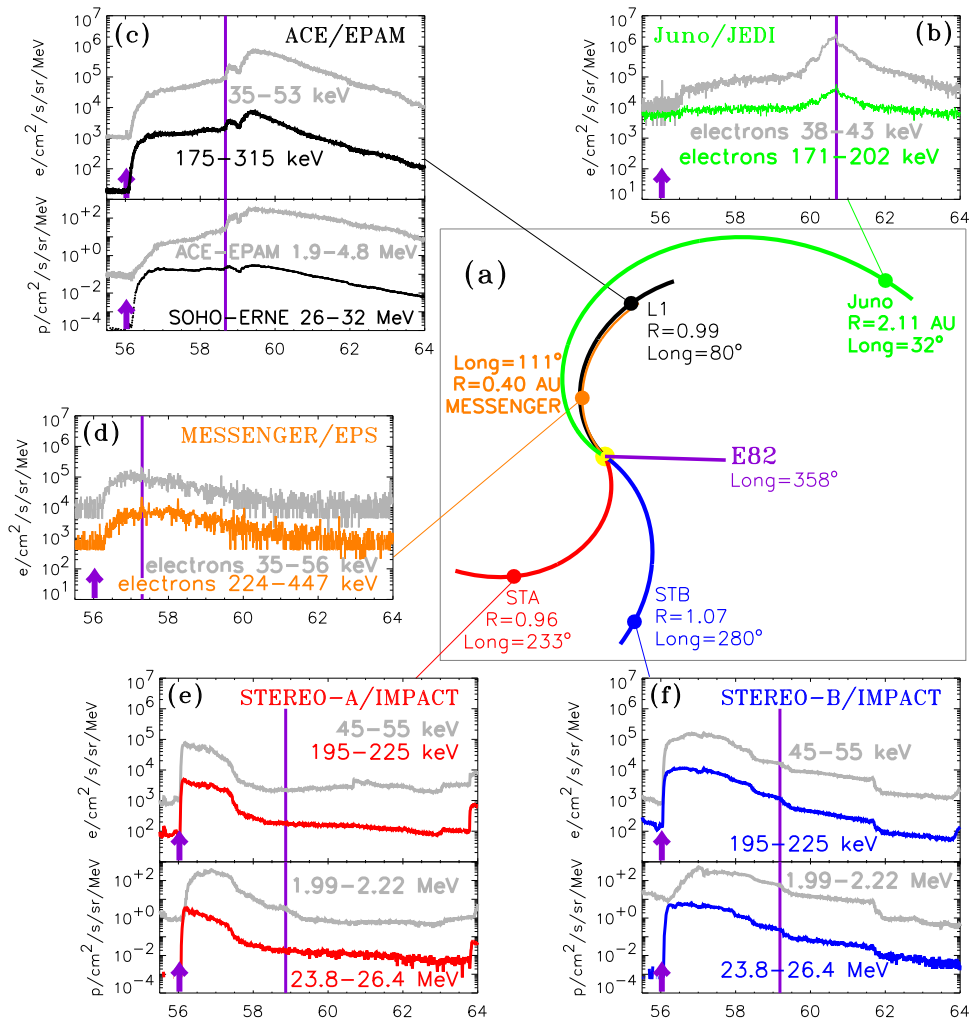


Figure 1. (a) View from the north ecliptic pole showing the location of *STEREO-A* (*STA*; red symbol), near-Earth observers (*L1*; black symbol), *STEREO-B* (*STB*; blue symbol), *MESSENGER* (orange symbol) and *Juno* (green symbol) on day 56 of 2014 (2014 February 25). R and Long indicate the heliocentric distance and heliocentric inertial longitude of each observer, respectively. Also shown are nominal interplanetary magnetic field lines connecting each spacecraft with the Sun (yellow circle at the center, not to scale) considering the solar wind measured at the onset of the SEP event (for *MESSENGER* and *Juno* we have considered the same speed as that measured at *L1*). The purple line indicates the longitude of the parent active region (E82° as seen from Earth, W125° as seen from *STEREO-A*, W78° as seen from *STEREO-B*, E113° as seen from *MESSENGER*, and E34° as seen from *Juno*). (b) 10-minute averages of near-relativistic electron intensities measured at *Juno*. (c) 10-minute average of near-relativistic electron (top) and proton intensities measured at *L1* by the *ACE* and *SOHO* spacecraft. (d) 10-minute average of near-relativistic electron intensities measured at *MESSENGER*. (e) 10-minute average of near-relativistic electron (top) and proton intensities measured at *STEREO-A*. (f) 10-minute average of near-relativistic electron (top) and proton intensities measured at *STEREO-B*. The purple arrows indicate the occurrence time of the parent solar flare and the purple vertical lines the passage of interplanetary shocks by each spacecraft.

et al. 1995) observed an asymmetric halo CME in association with this solar eruption with a plane-of-sky speed of 2147 km s^{-1} (Gopalswamy et al. 2015). The purple vertical lines in Figures 1(b)–(f) indicate the local passage of an IP shock observed by all the selected spacecraft that might be related to the shock initially driven by the CME.

In this paper, we analyze both (i) EUV and white-light coronagraph observations to investigate the solar phenomena associated with the origin of the SEP event, and (ii) in situ plasma and energetic particle observations from the selected spacecraft to determine both the extent of the associated IP shock and the properties of the SEP event at the different heliospheric locations. Section 2 describes the coronal magnetic field configuration existing prior to the SEP event and the estimated magnetic field connection established between each spacecraft and the Sun. In Section 3 we describe the solar observations that allow us to pinpoint the origin of the SEP event and determine the extent of the shock associated

with the CME as it started propagating away from the Sun. In Section 4 we characterize the properties of the SEP event at different longitudes and estimate the release times of the SEPs observed by each spacecraft. Section 5 discusses the possibility that the IP shock observed in situ by all the spacecraft had a common origin related to the origin of the SEP event. In Section 6 we determine the longitudinal and radial dependences of the observed SEP peak intensities. In Section 7 we specify the height and properties of the shock at the estimated SEP release times. Finally, Section 8 summarizes the main conclusions of the presented analyses.

2. SPACECRAFT MAGNETIC FIELD CONNECTIONS

Table 1 lists the locations of the spacecraft selected in this study and the footpoints of the field lines connecting each spacecraft with the Sun estimated using different methods. Specifically, columns 2–5 of Table 1 provide the heliocentric

Table 1
Spacecraft and Magnetic Footpoint Locations

Spacecraft	Spacecraft Location				Solar Wind Speed V_{sw} (km s ⁻¹)	Field Line Length L (au)	Field Line Footpoint Location					
	Location						Parker Spiral		PFSS		MAS	
	R (au)	Long	CL ^a	Lat			Long	Lat	Long	Lat	Long	Lat
(1)	(2)	(3)	(4)	(5)	(6)	(7)	(8)	(9)	(10)	(11)	(12)	(13)
<i>STEREO-B</i>	1.07	280°	25°	+7°	571	1.26	325°	+7°	317°	+15°	318°	+14°
Earth	0.99	80°	185°	-7°	426	1.14	136°	-7°	124°	-10°	126°	-9°
<i>STEREO-A</i>	0.96	233°	337°	+6°	372	1.10	294°	+6°	313°	+19°	315°	+12°
<i>MESSENGER</i>	0.40	111°	216°	-2°	426 ^b	0.41	133°	-2°	125°	-10°	129°	-10°
<i>Juno</i>	2.11	32°	137°	+1°	426 ^b	3.28	150°	+1°	126°	-11°	130°	-15°

Notes.

^a CL = Carrington Longitude.

^b For *MESSENGER* and *Juno* we assume the same solar wind speed as that measured at L1.

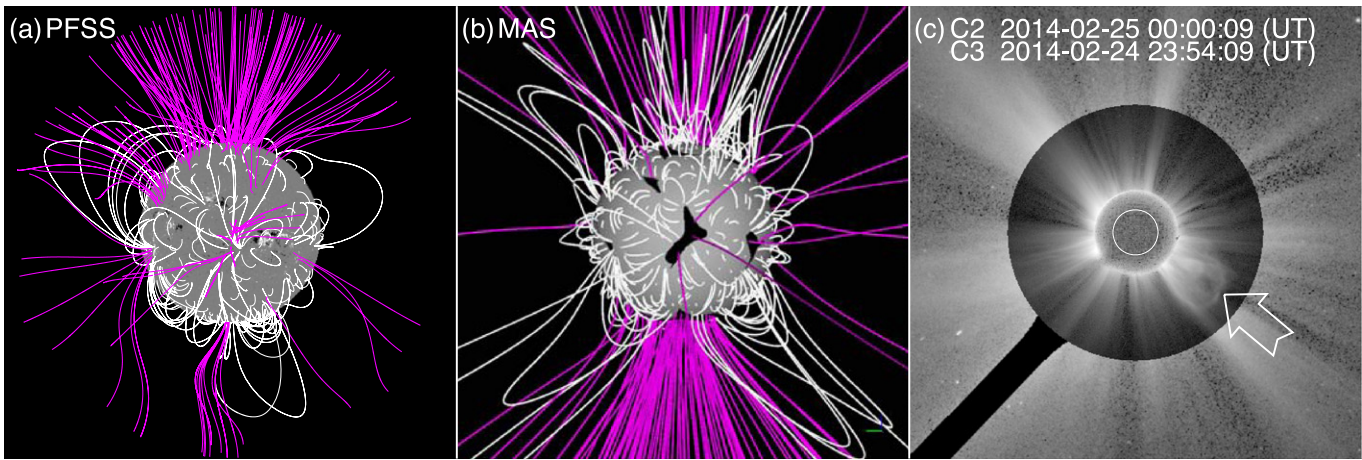


Figure 2. (a)–(b) Coronal magnetic field configuration as seen from Earth on 2014 February 25 at 00:04 UT obtained by (a) the PFSS model and (b) the MAS model. A selection of closed (white) and open (purple) field lines are shown. The black patches on the solar surface (at $1 R_{\odot}$) in panel (b) show the location of coronal holes. (c) Combination of images taken by the *SOHO/LASCO/C2* and *C3* coronagraphs showing the structure of streamers and the presence of a southwestward directed CME (indicated by the arrow) prior to the occurrence of the SEP event on 2014 February 25.

radial distance (R), the heliocentric inertial longitude (Long, also indicated in Figure 1(a)), the Carrington Longitude (CL) and the heliocentric inertial latitude (Lat), respectively, of *STEREO-B*, Earth, *STEREO-A*, *MESSENGER* and *Juno*. Figure 1(a) shows nominal Parker spiral magnetic field lines connecting each spacecraft with the Sun. Such field lines have been computed considering the solar wind speed V_{sw} measured at the onset of the SEP event (as listed in column 6 of Table 1). Owing to the lack of solar wind measurements from *MESSENGER* and *Juno*, we have assumed for these two spacecraft the same value of V_{sw} as that measured at L1. Note the close proximity between the nominal field lines connecting *MESSENGER*, *Juno* and L1 with the Sun. Column 7 of Table 1 lists the distance L between the Sun and each one of the spacecraft along these nominal Parker spiral lines. The heliospheric inertial coordinates of the magnetic footpoints of the nominal Parker spiral IMF lines are listed in columns 8 and 9 of Table 1.

The coordinates of the magnetic connection footpoints can also be estimated using the results of the “Magnetohydrodynamics outside A Sphere” (MAS) model (e.g., Riley et al. 2012). Such model solves the time-dependent, resistive MHD equations in spherical coordinates, and describes the large-scale behavior of the solar corona and inner heliosphere from the solar surface to $30 R_{\odot}$. It uses photospheric magnetic

field synoptic maps built up from a sequence of observations from the Helioseismic and Magnetic Imager (HMI; Scherrer et al. 2012) on board the *Solar Dynamics Observatory* (*SDO*; Pesnell et al. 2012) and determines the large-scale magnetic field structure of the corona. The details of the model can be found elsewhere (e.g., Riley et al. 2012, and references therein). Similarly, the potential field source surface (PFSS) model (Schatten et al. 1969) provides the large-scale coronal magnetic field topology at a distance below $2.5 R_{\odot}$ before the occurrence of the parent solar eruption. Figure 2 shows the magnetic field configuration of the corona as seen from Earth at 00:04 UT on 2014 February 25 as obtained by (a) the PFSS and (b) the MAS models. This time is immediately before the occurrence of the parent solar flare associated with the origin of the SEP event. The spherical surface, at $1 R_{\odot}$ in Figure 2(a), shows the location of the active regions (white and black spots) and a selection of closed (white) and open (purple) field lines computed by the PFSS model. The spherical surface, at $1 R_{\odot}$ in Figure 2(b), shows the location of the coronal holes (black surfaces) and a selection of closed (white) and open (purple) field lines computed by the MAS model. Figure 2(c) is a composite image combining images from the *C2* and *C3* cameras of *SOHO/LASCO* at the indicated times. The distribution of bright streamers shown in Figure 2(c) can be

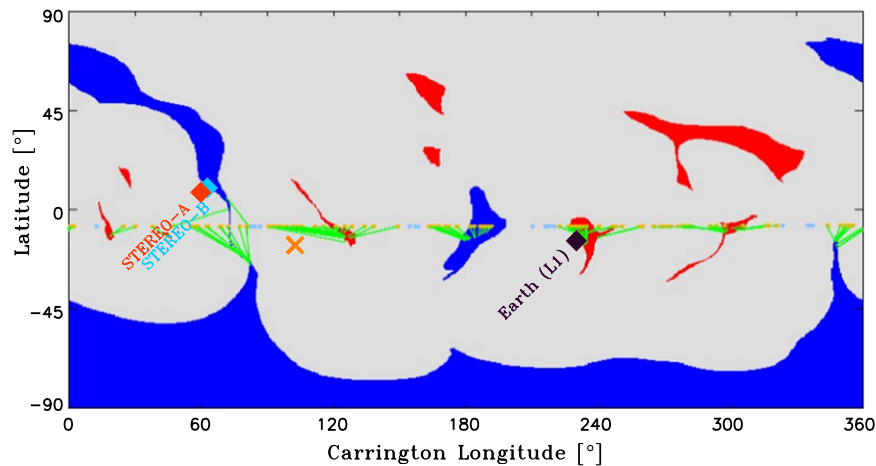


Figure 3. Coronal holes computed from the MAS simulation color-coded according to the observed underlying photospheric magnetic field (red for outward and blue for inward magnetic field polarity). Earth’s trajectory is superimposed (thin orange dots), together with the mapped source regions of the plasma measured at *ACE* (indicated by the green lines). Earth was at Carrington Longitude 185° at 00:39 UT on 2104 February 25. The black diamond identifies the footprint of the magnetic field line connecting to *ACE* at that time. We have also indicated with cyan and red diamonds the location of the footpoints of the field lines connecting to *STEREO-B* and *STEREO-A*, respectively. The orange cross identifies the site of the parent flare.

tracked back to the white closed field lines extending at high altitudes shown in Figure 2(b).

In order to estimate the magnetic connection footpoints of each spacecraft using the results of both the PFSS and the MAS models, we use the solar wind speed measured by each spacecraft (column 6 of Table 1) to ballistically track a nominal Parker spiral field line to a distance of $2.5 R_\odot$ for the PFSS model and to $30 R_\odot$ for the MAS model. This field line is then mapped back to the solar surface according to the magnetic field configurations shown in Figures 2(a) and (b). Columns 10 and 11 (12 and 13) of Table 1 show the estimated coordinates of the magnetic connection footpoints of each spacecraft using the PFSS (MAS) model. We see that both models agree, within a few degrees, in the location of the footpoints. Significant differences can be observed between the results of the PFSS and MAS models and those obtained using the Parker spiral projection, especially regarding the latitude of the footpoints and the longitude of the *STEREO-A* and *Juno* footpoints (the Parker IMF does not allow for latitudinal excursions of the IMF lines and neglects deviations of field lines close to the Sun due to the field configuration of the solar corona).

Figure 3 shows the coronal holes for Carrington Rotation 2147 (from day 42.7287 to day 70.0606 of 2014) computed from the MHD solution of the MAS model and color-coded according to the observed underlying photospheric field (red for outward and blue for inward). The units in the horizontal axis are degrees of the Carrington Rotation 2147 that can be transformed into heliocentric inertial longitude by subtracting $\sim 105^\circ$. Earth’s trajectory is superimposed (at latitude -7°) together with the mapped source regions of the plasma according to the solar wind speed measured at *ACE*. The thin green lines establish the connection between the ballistic projection at $30 R_\odot$ and the connecting point at $1 R_\odot$ through the field lines computed by the MHD model. The red, blue and black diamonds in Figure 3 identify the footpoints of the magnetic field lines connecting to *STEREO-A*, *STEREO-B* and L1 observers computed following the MAS method. Although *STEREO-A* and *STEREO-B* were physically separated by 47° in heliolongitude, and they observed solar wind of different speeds, their footpoints computed by both the PFSS and the MAS model were rooted to the same inward polarity coronal

hole, with the *STEREO-A* footpoint very close to the boundary of the modeled coronal hole. Magnetic field polarities observed at the onset of the SEP event at each spacecraft (see Section 4) agree with the modeled polarity found at the footpoint. The high-speed solar wind measured by *STEREO-B* at the onset of the SEP event (see Figure 9 below) resulted from the wake of a complex compound of ICMEs that crossed the spacecraft on 2014 February 20–22 (days of year 51–53). Figure 3 shows that the active region (orange cross) was well separated from the estimated location of the L1 magnetic connection footpoint.

Figure 2(c) shows the presence of a CME (in the C2 field of view) propagating in the southwest direction (indicated by the white arrow). This CME occurred prior to the main eruption responsible for the origin of the SEP event on 2014 February 25. It was first observed by *SOHO/LASCO/C2* at 23:24 UT on 2014 February 24 (day of year 55) and propagating with a plane-of-sky speed of 790 km s^{-1} (as reported in the LASCO CME catalog at cdaw.gsfc.nasa.gov/CME_list). No SEP intensity increase was observed in association with this CME by any of the spacecraft listed above. Applying the compound geometrical model developed by Kwon et al. (2014) to determine the three-dimensional (3D) structure of this CME using data from *STEREO*, *SDO* and *SOHO*, we infer that it propagated in the direction $S30^\circ W125^\circ$ (as seen from Earth), had a half-angle width of $\sim 30^\circ$, and its leading edge reached an altitude of $\sim 7\text{--}8 R_\odot$ from Sun center at the onset time of the X4.9/2B flare associated with the origin of the SEP event (i.e., 00:39 UT on 2014 February 25). Assuming a radial propagation of this prior CME, its origin was located at the heliocentric inertial longitude of 205° and covered at most a longitudinal range from 175° to 235° . Presumably, the presence of this prior CME distorted the field lines connecting to that region of the Sun. Therefore, we must indicate that, in principle, this CME was not wide enough to intercept the nominal IMF lines plotted in Figure 1(a) connecting each spacecraft with the Sun. However, if field lines differed from the nominal Parker spiral and this prior CME intercepted indeed the IMF lines connecting each spacecraft with the Sun, the site of the magnetic footpoints listed in Table 1 may differ from the actual magnetic connections existing prior to the SEP event.

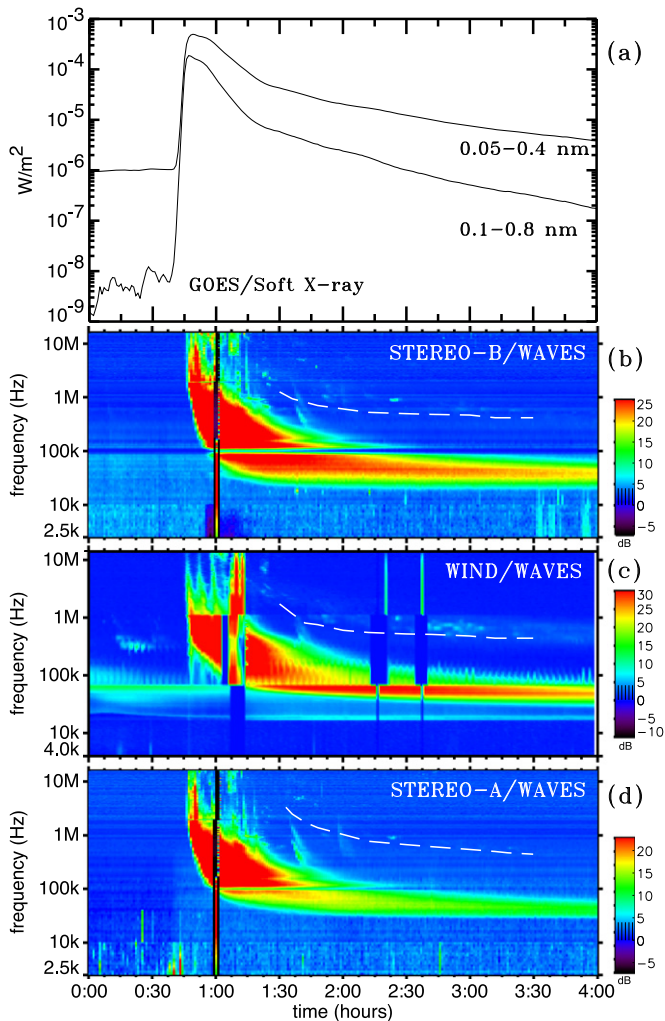


Figure 4. (a) *GOES* soft X-ray intensities. Radio measurements from (b) *SWAVES* on *STEREO-B*, (c) *WAVES* on *Wind*, and (d) *SWAVES* on *STEREO-A*. Dashed white lines indicate the Type II emission.

3. SOLAR OBSERVATIONS

Figure 4 shows, from top to bottom, (a) one-minute averages of the soft X-ray intensities measured by *GOES-15* and the intensities of the radio emissions as measured by (b) the *S/WAVES* detector (Bougeret et al. 2008) on *STEREO-B*, (c) the *WAVES* experiment (Bougeret et al. 1995) on *Wind*, and (d) the *S/WAVES* detector on *STEREO-A*. The origin of the SEP event was related to a *GOES* X4.9 flare starting at 00:39 UT and peaking at 00:49 UT. In the classification between gradual and impulsive solar flares used by Cane et al. (1986) and Kallenrode et al. (1992), this flare would have been classified as impulsive because of the short duration (~ 39 minutes) during which the 1–8 Å soft X-ray emission was above a factor 0.1 of the flare SXR peak intensity. This flare was also observed in hard X-rays by the *Reuven Ramaty High Energy Solar Spectroscopic Imager (RHESSI)* with onset at 00:37:04 UT and peak at 00:46:54 UT (Krucker & Hudson 2014) and in γ -rays by the *Gamma-ray Burst Monitor (GBM)* of the *Fermi Gamma-ray Space Telescope* with onset at 00:40:57 UT and peak at 00:52:58 UT (hesperia.gsfc.nasa.gov/fermi/gbm/qlook/fermi_gbm_flare_list.txt).

The site of the solar flare (S12E82) suggests that the spacecraft that was better connected, in terms of longitudinal

distance between the flare site and the footpoint of the nominal Parker spiral IMF line connecting each spacecraft with the Sun (cf. Figure 1(a)), was *STEREO-B* ($\Delta\psi \sim 33^\circ$), followed by *STEREO-A* ($\Delta\psi \sim 64^\circ$), the L1 observers and *MESSENGER* (both at $\Delta\psi \sim -138^\circ$), whereas the poorest connection was for *Juno* ($\Delta\psi \sim -152^\circ$) (where $\Delta\psi$ is the longitudinal separation between the flare site and the footpoint of the Parker IMF line connecting to each spacecraft as listed in column 8 of Table 1, and where negative values of $\Delta\psi$ indicate that the flare site was eastward of the nominal footpoint). Note that when using either the PFSS or the MAS models, the magnetic footpoints of both *STEREO-A* and *STEREO-B* were located in the same solar surface region that was separated $\sim 40^\circ$ in longitude from the flare site (Figure 3).

Figures 4(b)–(d) show that all three spacecraft at ~ 1 au observed type III radio bursts (starting after 00:45 UT) followed by type II radio bursts mainly visible from *STEREO-B* and *Wind*, but much weaker from *STEREO-A* (indicated by the dashed white lines in Figures 4(b)–(d)). Metric type III radio-bursts from ground-based observatories started at 00:45 UT. Metric type II emission was observed to start at 00:56 UT (ftp.swpc.noaa.gov/pub/warehouse/) indicating the presence of a shock moving from the low corona to IP space.

Images taken by the Atmospheric Imaging Assembly (AIA; Lemen et al. 2012) on board *SDO* during the solar eruption associated with the origin of the SEP event have been analyzed in detail by Long et al. (2015) and we refer the reader to this article for details. *SDO* observed an EUV wave that did not propagate across the visible hemisphere of the Sun but was confined to propagate along the eastern solar limb both northward and southward from the parent active region. The variations in Alfvén speed within the neighboring active regions constrained the propagation of the EUV wave (Long et al. 2015). Therefore, the EUV wave was never seen to reach the longitude of the magnetic footpoints of *MESSENGER*, *Juno* or near-Earth observers as estimated using the different methods described in Section 2. However, Figure 1 shows that an intense SEP event was observed at all these three locations.

An asymmetric halo CME was observed by *SOHO/LASCO* propagating mostly from the east limb of the Sun. It was first seen by *LASCO/C2* at 01:25 UT when the CME was already in progress (the prior *LASCO/C2* frame was taken at 00:48 UT). As seen from *LASCO*, the CME expanded enough to be classified as a full halo (plane-of-sky width of 360°) by 01:48 UT. We have applied the compound geometrical model developed by Kwon et al. (2014) to determine the 3D structure associated with the CME using EUV and white-light images from *STEREO*, *SDO*, and *SOHO*. An ellipsoid shape centered at a certain altitude h_E is used to describe the outermost front of the CME. Figures 5(a)–(c) show difference images from the coronagraph COR-1 of the Sun Earth Connection Coronal and Heliospheric Investigation (SECCHI, Howard et al. 2008) on board *STEREO-B*. The difference images were obtained by subtracting the image taken 5 minutes earlier from the image taken at the indicated time. We have overplotted in these images the outermost front represented by an ellipsoid by using red, orange, blue, and cyan colors (each color for each quadrant), whereas the white circles show the surface of the ellipsoid in 30° intervals. Dashed lines are used when the reconstructed structure is on the other side of the plane of the

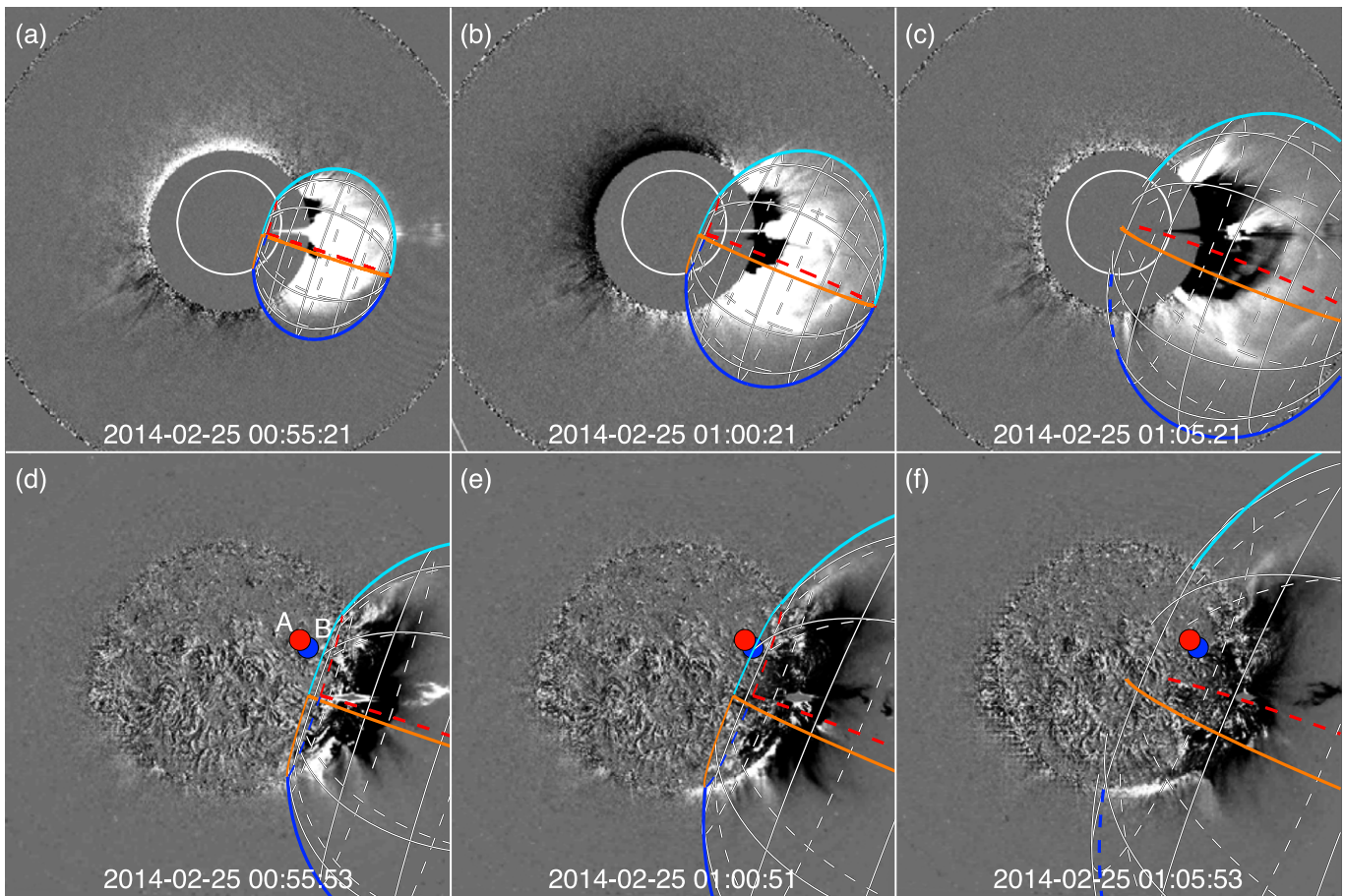


Figure 5. (Top) *STEREO-B/SECCHI/COR-1* and (Bottom) *STEREO-B/SECCHI/EUVI* 195 Å difference images obtained by subtracting the image taken 5 minutes earlier from the image taken at the indicated times. Overplotted is the position of the ellipsoid obtained by the model of Kwon et al. (2014) that best describes the 3D structure of the front shock ahead of the CME. Red, orange, blue and cyan colors represent each quadrant of the ellipsoid, whereas white circles are used to indicate the surface of the ellipsoid (dashed lines are used when the reconstructed structure is on the other side of the plane of the image). In the bottom panels, the blue and red symbols identify the footpoints of the magnetic field lines connecting to *STEREO-B* and *STEREO-A* using either the MAS or the PFSS models, respectively (the size used for the symbol covers the locations of the footpoints estimated using both models). For the image at 01:05 (right panels) the EUV wave was not observed anymore and the ellipsoid was obtained by just fitting the white-light coronagraph images.

image. Figures 5(d)–(f) show difference images from the Extreme Ultraviolet Imager (EUVI) of *STEREO-B/SECCHI* at 195 Å (Wueller et al. 2004) obtained using the same technique described above for Figures 5(a)–(c). We see that the EUV wave front reached the magnetic footpoints of both *STEREO-B* and *STEREO-A* estimated using both the MAS and the PFSS models (blue and red symbols in Figures 5(d)–(f)) around ~01:00 UT (Figure 5(e)). After that time, however, the EUV wave was not seen to propagate eastward (from *STEREO-B*'s point of view). The footprint of the ellipsoid over the solar surface coincides with the EUV front for times prior to 01:05 UT (as seen in the images in Figures 5(d) and (e)). At 01:05 UT (Figure 5(f)) the EUV wave was no longer observed and the ellipsoid was obtained by just fitting the white-light images. For the magnetic footpoints estimated using a simple Parker spiral projection, the EUV wave reached the footpoint of *STEREO-B* at ~00:55 UT but it never reached the estimated location of the footpoint of *STEREO-A*. Therefore, as seen from *STEREO-B*, the extent of EUV wave projected over the solar disk was also very limited.

Figure 6 shows, for different times, representations of the outermost front of the CME overplotted in a combination of images taken by *STEREO/SECCHI/COR-1*, *COR-2*, *EUVI*,

SDO/AIA and *SOHO/LASCO/C2* and *C3* (first three columns). The major axis of the ellipsoid was directed toward S14E76 at 00:46 UT (when its leading edge was at $0.4 R_{\odot}$ above the solar surface) and at S19E91 at 01:54 UT (when its leading edge was at $12.7 R_{\odot}$ above the solar surface). Whereas the eastern portion of the shock front ahead of the CME (as seen from L1) took the shape of an ellipsoid, the white light emission in the western longitudes (as seen from L1) seemed to be disconnected from the eastern portion (e.g., Figures 6(f) and (j)). Figure 7 shows a difference image from *SOHO/LASCO/C2* identifying a faint front (indicated by the white arrows) at the latitudes where the ellipsoid shown in Figure 6 overestimates the altitude of the outermost front driven by the CME. This faint front results from the imprint on the plane-of-sky images of streamers deflected by the passage of the shock wave (see similar examples in Vourlidis et al. 2013). In fact, the images clearly show (e.g., Figure 6(f)) that the passage of the shock front over the west limb of the Sun (as seen from L1) was able to deflect the streamers located over the northwest and southwest quadrants shown in Figure 2(c). The conditions of propagation of a shock wave within streamers are different from the propagation conditions in other regions of the corona and hence that the shock front moving over the west limb of the

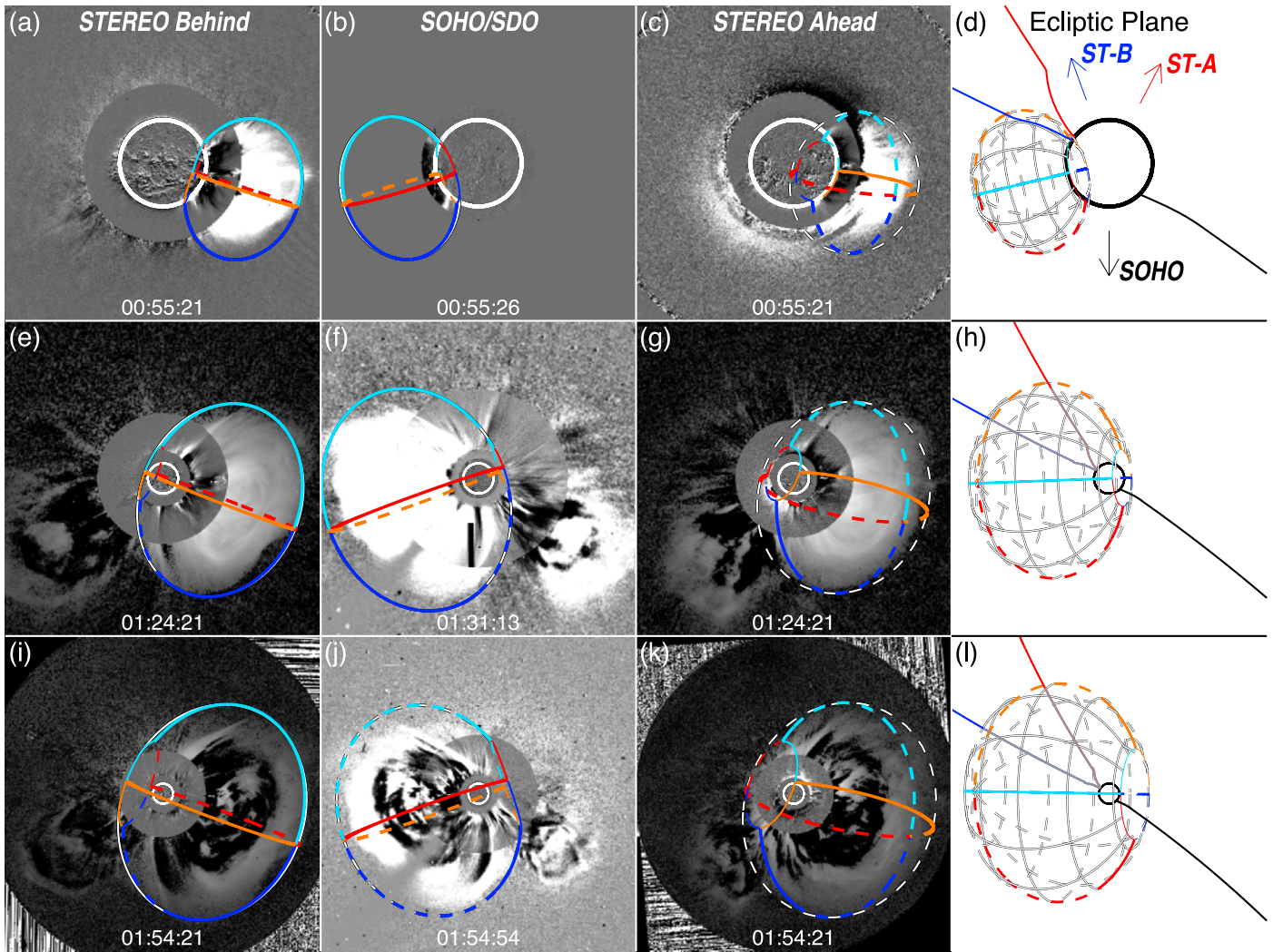


Figure 6. First three columns: selected time series observations of the CME in composite images taken by *STEREO-B*, *SDO* and *SOHO*, and *STEREO-A* (from left to right). The solar center is located at the center of each panel and the solar rotational axis is the north of each image. The white circle in each panel refers to the solar disk. Images at the center of each panel are running difference images from *STEREO/SECCHI/EUVI* 195 Å in the first and third columns and running ratio images from *SDO/AIA* 193 Å in the second column. White light observations are running difference images from *STEREO/SECCHI/COR-1* and *STEREO/SECCHI/COR-2* in the first and third columns and *SOHO/LASCO/C2* in the second column. The representations of the reconstructed 3D shock front are indicated by the red, orange, blue and cyan lines whereas the white line shows the maximum extension of the shock front. Dashed lines are used when the 3D structure is located in the other side of the plane of the image. Right Column: projection of the ellipsoid shock front in the ecliptic plane as seen from the north ecliptic pole. The red, blue and black lines indicate the magnetic field lines connecting to *STEREO-A*, *STEREO-B* and *L1*, respectively, computed assuming Parker IMF lines above $2.5 R_{\odot}$ and the PFSS configuration below $2.5 R_{\odot}$ (gray color is used for the portion of the field line inside the modeled ellipsoid).

Sun (as seen from *L1*) is not well represented by the fitted ellipsoid. Therefore, we will characterize the passage of the shock front over western longitudes (as seen from Earth) by the faint front identified in Figure 7, whereas the fitted ellipsoid provides an adequate identification of the shock location at eastern longitudes. For this reason, the portion of the ellipsoid propagating over western longitudes (as seen from Earth) or over eastern longitudes (as seen from the two *STEREO* spacecraft) is not represented in Figures 6(i)–(k).

The right column of Figure 6 shows the ellipsoid projection on the ecliptic plane as seen from the north ecliptic pole. We have also plotted IMF lines connecting to *STEREO-B* (blue), *STEREO-A* (red) and *SOHO* (black) estimated using the nominal Parker spiral IMF lines up to a heliocentric distance of $2.5 R_{\odot}$ and then using the PFSS model (the black circle indicates the distance $1 R_{\odot}$). The bend of the field lines in Figure 6(d) occurs at the intersection between the outer

boundary of PFSS and the point where the Parker spiral field line is assumed. The arrows in Figure 6(d) indicate the radial direction to each spacecraft. Note that the passage of the shock most likely implied a change in the direction of the field lines; therefore we plot these field lines in gray when they remain inside the fitted ellipsoid, whereas the colored portion of the field lines in Figures 6(d), (h) and (l) indicate the field configuration found upstream of the shock as it expanded away from the Sun. For the reasons shown in Figure 7, the portion of the ellipsoid at the western longitudes (as seen from Earth), i.e., the longitudes where *L1* observers establish magnetic connection has not been plotted. We should note that at the time of the solar eruption, the field configuration provided by the PFSS and MAS models may be destabilized; therefore the field configuration shown in Figure 6(d) is only a crude approximation of the existing field prior to the solar eruption that the

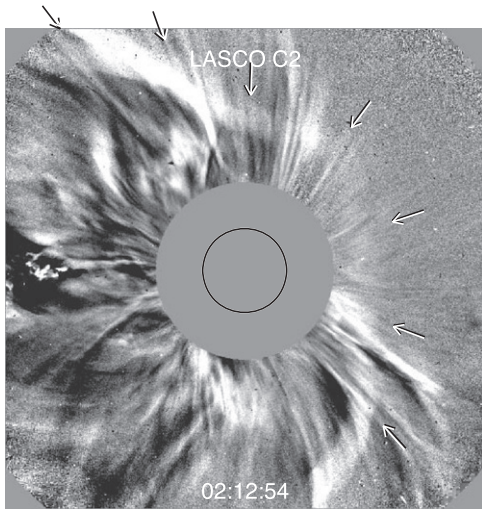


Figure 7. *SOHO*/LASCO/C2 difference image obtained from the images taken at 02:00:54 and 02:12:54 UT. The white arrows indicate the location in the plane-of-sky of the portion of the shock front moving westward (as seen from Earth) that did not follow the same evolution as the eastward front fitted with the ellipsoid. Northwest and southwest streamers shown in Figure 2(c) experienced significant deflection as the CME expanded over these latitudes. As discussed in the text, the front of the CME was distorted from an ellipsoid due to the different propagation conditions in this region.

traveling shock will find upstream as it expands away from the Sun.

4. IN SITU ENERGETIC PARTICLE AND MAGNETIC FIELD OBSERVATIONS

The in situ instrumentation on board the selected spacecraft provides us with both energetic particle and magnetic field measurements that allow us to characterize the SEP event at different longitudinal and radial distances. Whereas spacecraft at ~ 1 au provide energetic particle measurements of both electrons and ions as well as solar wind plasma observations, the observations from *MESSENGER* and *Juno* were limited to just magnetic field and near-relativistic electron measurements. Here we analyze in detail the in situ observations from each location.

4.1. The SEP Event at ~ 1 au

Figure 8 shows a collection of energetic particle intensities measured at ~ 1 au by (from left to right) *STEREO-B*, *STEREO-A* and near-Earth spacecraft (*SOHO* and *ACE*) during the SEP event on 2014 February 25. From top to bottom we show 10-minute averages of (a) >13 MeV proton intensities in several differential energy channels, (b) near-relativistic and relativistic electron intensities, and (c) hourly averages of ~ 500 keV/n and ~ 18 MeV/n Fe and O intensities. Proton intensities (Figure 8(a)) were measured by IMPACT/HET onboard *STEREO* and by ERNE onboard *SOHO*. Near-relativistic electron intensities (red traces in Figure 8(b)) at both *STEREO-A* and *STEREO-B* were measured by IMPACT/SEPT and by the Deflected Electron (DE) system of EPAM (Gold et al. 1998) on board *ACE*. Relativistic electron intensities (blue traces in Figure 8(b)) at the two *STEREO* spacecraft were measured by the IMPACT/HET and near Earth by the Electron Proton Helium instrument (EPHIN; Müller-Mellin et al. 1995) onboard *SOHO*. Finally, the

~ 18 MeV/n Fe and O intensities (Figure 8(c)) at the two *STEREOs* were measured by the Low Energy Telescope (LET; Mewaldt et al. 2008) and at *ACE* by the Solar Isotope Spectrometer (SIS; Stone et al. 1998), whereas the ~ 500 keV/n Fe and O intensities were measured by the Suprathermal Ion Telescope (SIT; Mason et al. 2008) on board *STEREO* and by the UltraLow Energy Isotope Spectrometer (ULEIS; Mason et al. 1998) on board *ACE*. The SEP event was very energetic, observed even at >100 MeV proton energies by *GOES-13* (not shown here) and at >60 MeV proton energies by *STEREO-A* and *STEREO-B*.

The high-energy proton and electron intensity increase was very abrupt at the two *STEREO* spacecraft whereas the increase was more gradual at L1. The prompt component of the SEP event (i.e., the first portion of the intensity-time profiles observed shortly after the occurrence of the parent solar flare and when the CME-driven shock is still close to the Sun) seem to be ordered in terms of the longitudinal distance $\Delta\psi$ between the nominal Parker IMF connecting footpoint and the flare site. The larger peak intensities of the prompt component were observed at *STEREO-B* ($\Delta\psi \sim 33^\circ$), followed by *STEREO-A* ($\Delta\psi \sim 64^\circ$), and lower values at L1 ($\Delta\psi \sim -138^\circ$). Note that no intercalibration correction factors between the intensities of the different instruments found in prior studies (e.g., Figure 2 in Lario et al. 2013 or Figure 3 in Richardson et al. 2014) have been applied in Figure 8. Such factors would imply a decrease in the *SOHO*/EPHIN and *ACE*/EPAM/DE electron intensities which favors the fact that particle peak intensities in the prompt component of the event at L1 were lower than at the two *STEREO* spacecraft.

According to the PFSS and MAS models the footpoints of both *STEREOs* were very close in longitude (cf. Table 1) implying that, if the particle injection occurs close to the magnetic footpoint, the differences in the particle intensities observed at the onset of the event by both *STEREOs* should be smaller than those predicted by the nominal values of $\Delta\psi$. However, if the field lines connecting to each spacecraft diverge with heliocentric distance (as shown in Figure 6(d)), the differences of the particle intensity-time profiles at *STEREO-A* and *STEREO-B* reside in the portion of the CME-driven shock that connects to each spacecraft as the shock expands.

Figure 8(c) shows that the ~ 18 MeV/n Fe/O ratio at the time of the peak intensity was about ~ 0.53 , ~ 0.44 at *STEREO-B* and *STEREO-A*, respectively; whereas the ~ 500 keV/n Fe/O ratio at the time of the Fe peak intensity was ~ 1.28 and ~ 0.73 at *STEREO-B* and *STEREO-A*, respectively. From the *ACE* point of view, ion intensity-time profiles differ between low and high energies. Whereas at high energies a first peak intensity in the Fe intensities is observed early on day 57 (where the ~ 18 MeV/n Fe/O ratio was ~ 0.67), the largest oxygen intensities are observed after the passage of the shock passage (where the ~ 18 MeV/n Fe/O ratio decreased to ~ 0.20). At low energies a gradual intensity increase is observed before the shock passage where the ~ 500 keV/n Fe/O ratio was about ~ 0.06 (measurable when Fe intensities were above ULEIS sensitivity; G. M. Mason (2015, private communication)). Low-energy ion intensities increase after the shock (where the ~ 500 keV/n Fe/O ratio was about ~ 0.12). The Fe/O ratios at both low and high energies at *STEREO-B* and *STEREO-A* were significantly higher than the event-averaged Fe/O ratios measured in large gradual SEP events (e.g.,

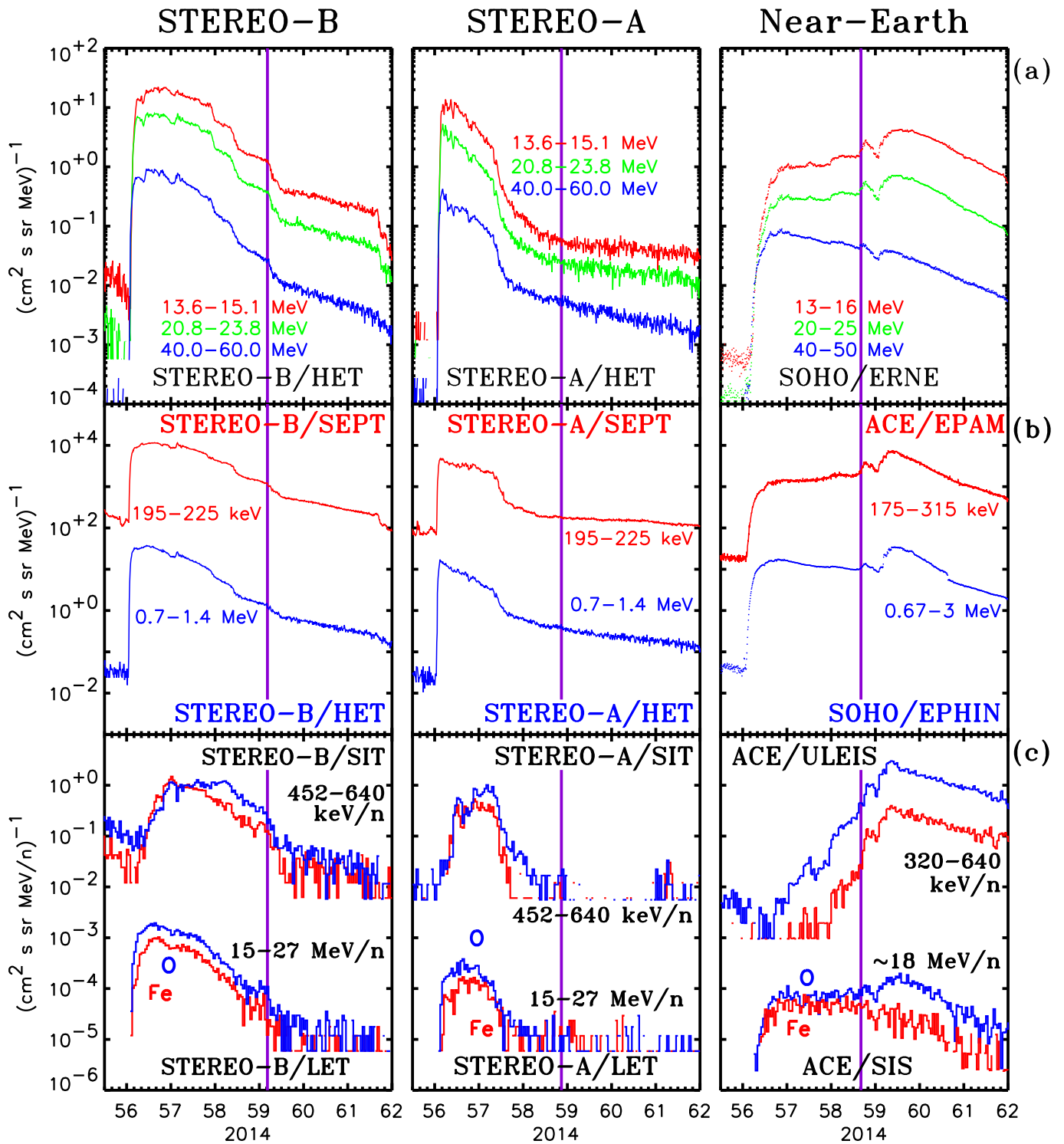


Figure 8. Intensity-time profiles of, from top to bottom, protons, electrons and heavy ions, as measured by, from left to right, *STEREO-B*, *STEREO-A* and L1 observers. The purple vertical lines indicate the time of the local passage of an interplanetary shock.

Fe/O \sim 0.134 at 5–12 MeV/n as determined by Reames 1995 or Fe/O \sim 0.404 at \sim 380 keV/n as determined by Desai et al. 2006). The high-energy Fe/O ratio measured at *ACE* during the prompt component of the event was also considerably higher than average abundances, whereas at low energies the dominance of the particle intensities behind the shock led to lower Fe/O ratios. Therefore, high-energy intensities measured early in the event at the three locations can be considered

Fe-rich, whereas at low-energies the SEP event was clearly Fe-rich at both *STEREOs* but not at *ACE*.

The differences in the intensity-time profiles observed by the three spacecraft reside in (i) the properties of the particle sources connected to each spacecraft, (ii) how and when the different spacecraft establish magnetic connection with the portion of the traveling CME-driven shock able to inject SEPs, and (iii) the properties of the medium that allows SEPs to

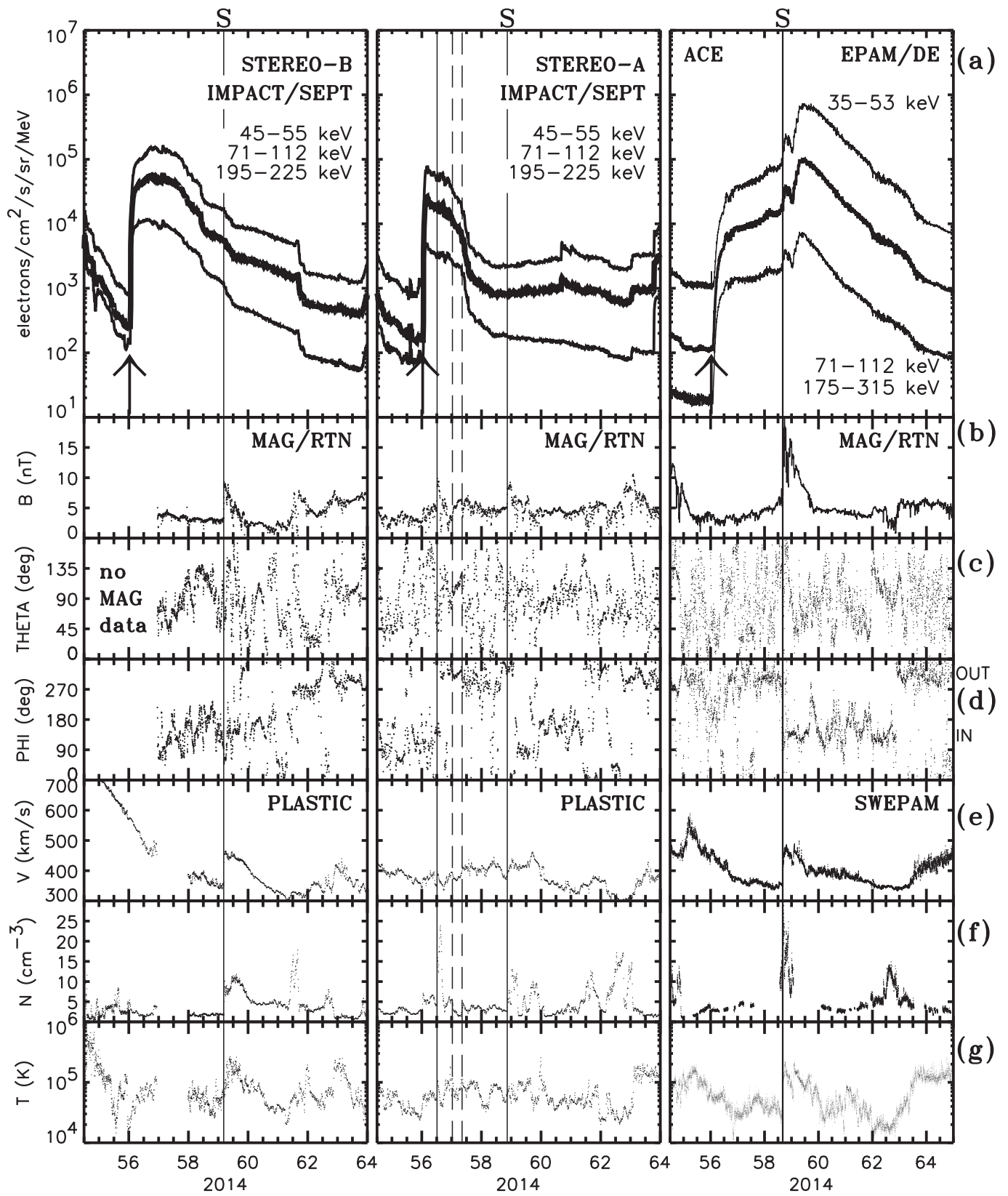


Figure 9. In situ observations at ~ 1 au as observed, from left to right, by *STEREO-B*, *STEREO-A* and *ACE*. From top to bottom, (a) electron intensities, (b) magnetic field magnitude, (c)–(d) magnetic field angular direction in the RTN coordinate system, (e) solar wind speed, (f) solar wind proton density, and (g) solar wind temperature. The solid vertical lines indicate the passage of interplanetary shocks, and the dashed vertical lines the passage of an ICME by *STEREO-A*.

propagate from their source to each spacecraft. Figure 9 shows a collection of in situ observations measured at ~ 1 au by (from left to right) *STEREO-B*, *STEREO-A* and *ACE*. From top to bottom we show: (a) one-minute averages of electron intensities at different energies as measured by IMPACT/SEPT on *STEREO* and by EPAM/DE on *ACE*, (b) the magnetic field magnitude as measured by the magnetometer of the IMPACT suite of instruments on board *STEREO* (Acuña et al. 2008) and the magnetic field experiment on board *ACE* (Smith et al. 1998), (c) the elevation angle of the magnetic field vector in the RTN coordinate system, (d) the azimuth angle of the magnetic field vector in the RTN coordinate system (for a spacecraft at ~ 1 au and a solar wind of 400 km s^{-1} , $\sim 315^\circ$ correspond to outward directed magnetic field whereas $\sim 135^\circ$ is for an inward magnetic field; indicated by OUT and IN in Figures 9(d)), (e) the solar wind speed, (f) solar wind proton density, and (g) solar wind proton temperature as measured by the PLASTIC instrument on board *STEREO* (Galvin et al. 2008) and the SWEPAM instrument on board *ACE* (McComas et al. 1998). In order to compare with the electron intensities measured at *MESSENGER* (Section 4.2), we have added in Figure 9(a) one minute averages of 71–112 keV electron intensities (thick black line) obtained from the energy spectra formed from the energy channels of *STEREO*/IMPACT/SEPT and *ACE*/EPAM/DE.

The solid vertical lines in Figure 9 identify the passage of interplanetary shocks and the dashed vertical lines the passage of an interplanetary counterpart of a CME by *STEREO-A* as identified by L. Jian (see www-ssc.igpp.ucla.edu/forms/stereo/stereo_level_3.html and Jian et al. 2013). Assuming that the shock labelled with the letter S in Figure 9 observed by *STEREO-B* at 59/04:24 UT, *STEREO-A* at 58/20:47 UT and *ACE* at 58/16:08 UT originated at the Sun at the time of the X4.9 flare (00:39 UT), we infer an average transit speed of ~ 587 , 585 and 648 km s^{-1} to travel from the Sun to *STEREO-B*, *STEREO-A* and L1, respectively. The passage of this shock by each spacecraft was indicated by the vertical purple lines in Figures 1 and 8. In terms of the density and magnetic field compression ratios (r_n and r_B) computed using values of the solar wind density and field magnitude before and after the shock passage, the shock strength was slightly larger at *ACE* ($r_n \sim 2.4$, $r_B \sim 2.8$) and *STEREO-B* ($r_n \sim 3.5$, $r_B \sim 2.2$) than at *STEREO-A* ($r_n \sim 2.1$, $r_B \sim 1.5$). Assuming that the nose of the shock driven by the CME on 2014 February 25 was centered at the longitude of the associated flare E82 (heliocentric inertial longitude -2°), and that the shock observed in situ by the three spacecraft was indeed driven by this CME, the shock would have had a width at 1 au of $\sim 125^\circ$ (to be observed by *STEREO-A*, or by symmetry around the flare site $\sim 250^\circ$), $\sim 78^\circ$ (to be observed by *STEREO-B*, or by symmetry around the flare site $\sim 156^\circ$), and $\sim 82^\circ$ (to be observed by *ACE*, or by symmetry around the flare site $\sim 164^\circ$). Note that after the passage of the shock S no clear signatures of ICME were observed near Earth (see ICME list compiled by Richardson & Cane at www.srl.caltech.edu/ACE/ASC/DATA/level3/icmetable2.htm). *STEREO-B* observed a decline in the solar wind speed after the passage of the shock S that together with the evolution of the thermal plus magnetic field pressure (L. Jian 2015, private communication) resemble those structures associated with the passage of post-shock structures where the shock and sheath regions were observed but the ICME itself passed far away from the spacecraft (i.e., Group 3 in the ICME

classification of Jian et al. 2006). After the passage of the shock S by *STEREO-A*, intermittent bidirectional 73–194 eV electron fluxes were observed early on day 60, which may indicate the passage of some structure resembling an ICME although no other signatures of an ICME were observed (see stereo.cesr.fr and www-ssc.igpp.ucla.edu/forms/stereo/stereo_level_3.html).

The second particle intensity increase observed by spacecraft at L1 early on day 59 (i.e., after the passage of the shock) was very prominent at electron intensities and at both low-energy proton and ion intensities, as well as high-energy oxygen intensities. This increase did not show any velocity dispersion effect, leading us to believe that it was due to a spatial structure formed behind the shock that was able to confine low-rigidity particles. In fact, the right column of Figure 9 shows that this new intensity increase was observed as solar wind density, speed and magnetic field decreased after the passage of the compressed region formed behind the shock.

In order to confirm the arrival direction of the particles at the onset of the event, Figure 10 shows the near-relativistic electron anisotropy information in the energy range ~ 50 – 80 keV as seen by (left) *STEREO-A*/SEPT and (right) the Silicon Semiconductor Telescopes (SST) of the 3D Plasma and Energetic Particle instrument (3DP) on board *Wind* (Lin et al. 1995). The SEPT instrument consists of four identical telescopes mounted to cover four viewing directions that are to the north, to the south, along the nominal Parker spiral to the Sun, and along the nominal Parker spiral away from the Sun (Müller-Mellin et al. 2008). The coverage of pitch angles by these four telescopes depends on the orientation of the magnetic field. Similarly, the multiple angular sectors used by the 3DP/SST on board the spin-stabilized *Wind* spacecraft allow us to determine pitch-angle distributions of near-relativistic electrons near Earth. In particular, we use *Wind*/3DP/SST electron intensities downloaded from sprg.ssl.berkeley.edu/wind3dp/ that are already sorted into eight pitch-angle bins. The top panels of Figure 10 show electron pitch-angle distributions color coded according to the measured intensity (indicated by the top color bar) and divided into four pitch-angle bins for *STEREO-A* (left) and eight for *Wind*/3DP (right). The second panel shows the orientation in pitch-angle space of the center point of the field of view of each of the four telescopes of *STEREO*/SEPT (left), and of each of the eight pitch-angle bins provided in the *Wind*/3DP/SST data files (right) that allows us to determine the pitch-angle coverage of each instrument. The third panel shows the intensity measured in each one of the four telescopes in the case of *STEREO*/SEPT, and in each one of the eight pitch-angle bins in the case of *Wind*/3DP/SST. The fourth panel shows the first-order anisotropy coefficient defined as $A = 3 \int_{-1}^{+1} I(\mu) \mu d\mu / \int_{-1}^{+1} I(\mu) d\mu$, where $I(\mu)$ is the pitch-angle-dependent intensity measured in a given viewing direction and μ is the average pitch-angle cosine for that direction. Details of how this anisotropy coefficient is computed can be found in Dresing et al. (2014, and references therein). The sign of A is given in terms of the magnetic field polarity which was inward at the onset of the event for both *STEREO-A* and *Wind*. Note that although near-Earth observers were immersed in a global outward magnetic field sector (see Figure 3), Figure 9(d) shows that at the onset of the event the magnetic field turned radial with inward polarity. Hence the negative values of A in

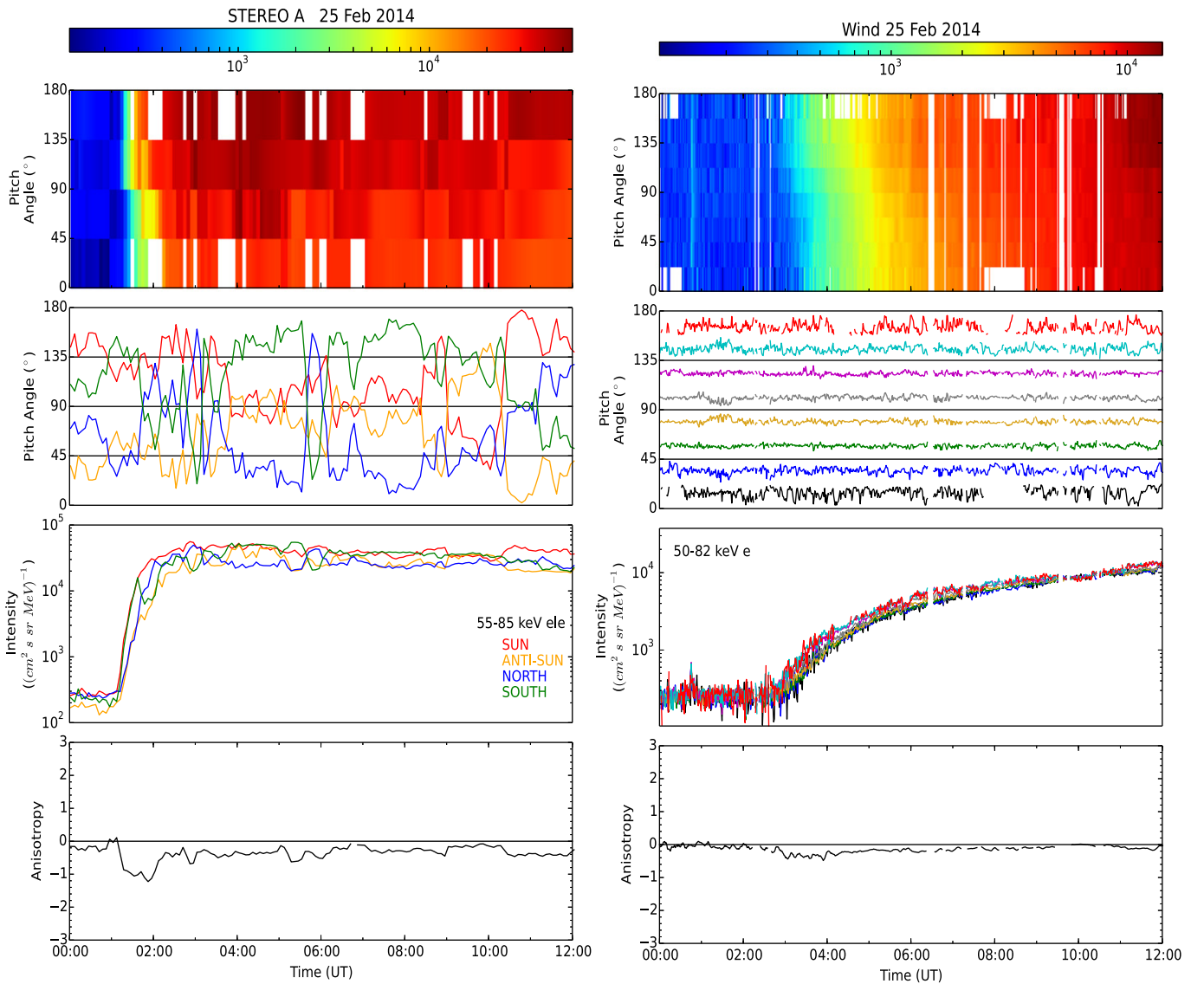


Figure 10. Anisotropy and intensity time profiles of near-relativistic electrons as observed by *STEREO-A* (left) and *Wind* (right). From top to bottom: pitch-angle dependent intensity distribution color coded according to the intensity indicated in the top horizontal color bar (units are electrons $\text{cm}^{-2} \text{sr}^{-1} \text{s}^{-1} \text{MeV}^{-1}$). Pitch-angle direction measured at the center of the four telescopes of *STEREO-A*/SEPT (Sun/red), anti-Sun (orange), north (blue), and south (green)), and of the 8 pitch-angle bins of *Wind*/3DP/SST. Intensity measured in each one of the four telescopes of *STEREO*/SEPT and each one of the 8 pitch-angle bins of *Wind*/3DP/SST. First-order anisotropy A . The energies covered are 55–105 keV for *STEREO-A* and 58–82 keV for *Wind*.

Figure 10 indicate antisunward particle flows at both spacecraft during the onset of the event.

Figure 10 shows that the onset of the event was more anisotropic at *STEREO-A* than at *Wind* and that it occurred earlier at *STEREO-A* than at L1 suggesting that either the magnetic connection with the particle source at the onset of the event was better established for *STEREO-A* than for *Wind* (cf. Figure 4 in Heras et al. 1994) or that the particles propagating toward *STEREO-A* experienced less scattering than those propagating toward L1. If the onset of the event at *Wind* resulted from a continuous injection of particles by a traveling shock establishing better connection with the spacecraft, the SEP event results in a gradual increase with lower anisotropies than the case when the magnetic connection with an intense particle source is abruptly established. The lack of magnetic field data at the onset of the event at *STEREO-B* prevents us from computing pitch-angle distributions at this spacecraft. However, inspection of data from the different telescopes of

SEPT (not shown here) allows us to see an anti-sunward dominated electron flow during the rise of the event.

In order to estimate the release times of the SEPs we apply the velocity dispersion analysis (VDA) method to the onset times of the energetic particle intensity enhancements observed at the different spacecraft (e.g., Vainio et al. 2013). Figure 11 shows such onset times as observed by, from right to left, (a) *STEREO-B*, (b) *STEREO-A* and (c) L1 observers as a function of $c/v = 1/\beta$ where v is the particle speed. The green diamonds indicate the onset time of the proton event as seen by the HET instrument on *STEREO* (Figures 11(a) and (b)) and by the ERNE instrument on *SOHO* (Figure 11(c)) and identified using the Poisson-CUSUM method developed by Huttunen-Heikinmaa et al. (2005). The black symbols in Figures 11(a) and (b) indicate the onset of the electron event as seen by the 0.7–1.4 MeV electron channel of HET on *STEREO* and by the 375–425 keV electron channel of the telescope of the SEPT instrument showing an earlier increase. The black

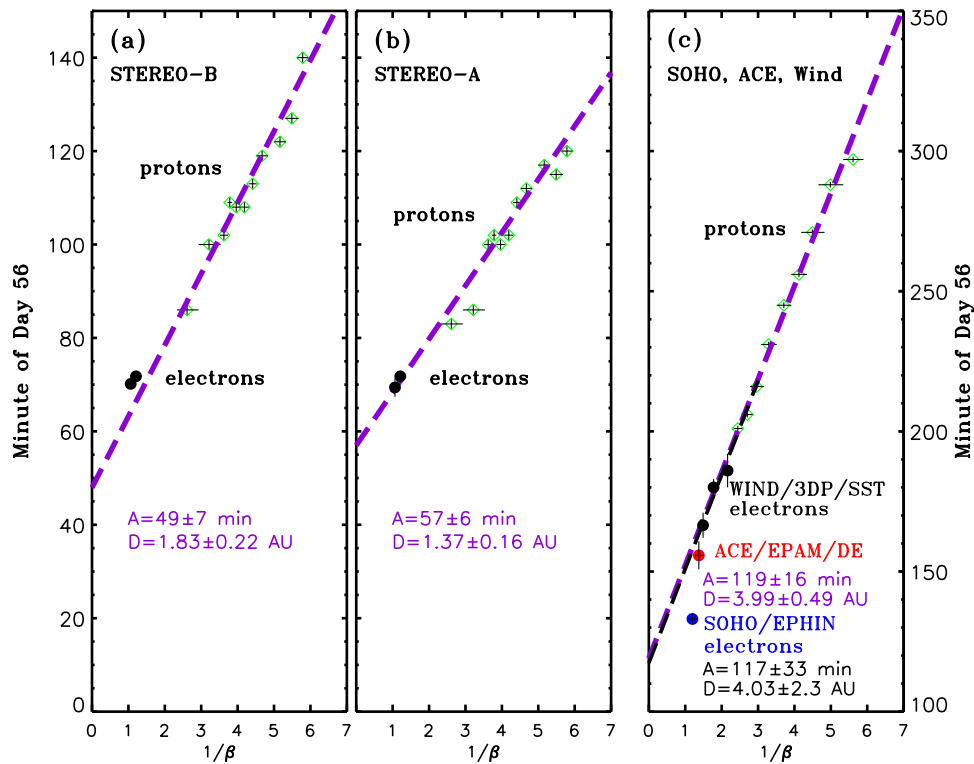


Figure 11. Velocity dispersion analysis of the onset of the SEP event at (left) *STEREO-B*, (center) *STEREO-A*, and (right) L1. The green symbols identify the proton onsets. The black symbols in the left and middle panel identify the onsets of the event as observed by the 375–425 keV electron channel of *STEREO*/SEPT and the 0.7–1.4 MeV electron channel of *STEREO*/HET. The black symbols in the right panel identify the onset of the event as observed in different energy channels of *Wind*/3DP/SST, the red symbol the onset in the 175–315 keV electron channel of *ACE*/EPAM/DE and the blue symbol in the 0.25–0.70 MeV electron channel of *SOHO*/EPHIN. The purple dashed lines are linear regression fits to all proton data points and the dashed black line to *Wind*/3DP electron data points. The legend gives the estimated release time (A) and the path length (D) discussed in the text.

symbols in Figure 11(c) indicate the onset times in the energy range ~ 50 –210 keV as measured by the different electron channels of *Wind*/3DP/SST in the pitch-angle bin that shows the earliest increase (we have applied the approach described by Wang 2009 to correct the *Wind*/3DP/SST intensities for contamination produced by $\sim 15\%$ of incident electrons that scatter out of the silicon detector of the SST telescope). We also indicate in Figure 11(c) the onsets in the 175–315 keV electron channel of *ACE*/EPAM/DE (red symbol) and the 0.25–0.70 MeV electron channel of *SOHO*/EPHIN (blue symbol). The purple dashed lines in Figure 11 are a least-square fit to the proton onset times at different energies given by the expression $t_i = A + D/v_i$, where t_i is the onset time in the energy channel detecting particles of speed v_i (considered to be the speed of particles with energy equal to the geometrical mean of the energy window of the channel, and considering the error bars in the identification of the event onsets ± 2 minutes and the energy window of each channel), A is the release time of the particles at the Sun, and D the effective path length traveled by these particles.

The estimation of the release time by the VDA method assumes (1) the onset of the SEP injection profile is both impulsive and energy independent, and (2) the first arriving particles observed at the spacecraft propagate scatter-free, with a pitch-angle cosine $\mu = 1$, along a common travel distance D from their coronal injection site to the spacecraft. The intercept of the purple straight lines in Figure 11 with the vertical axis gives an estimate of the release time of protons observed by *STEREO-B* at $A = 49 \pm 7$ minutes (i.e., 00:57 UT ± 7 minutes adding ~ 8 minutes of the light transit time to directly compare

with the electromagnetic observations described in Section 3), by *STEREO-A* at $A = 57 \pm 6$ minutes (i.e., $\sim 01:05$ UT ± 6 minutes adding the light travel time), and by *SOHO* at $A = 119 \pm 16$ minutes (i.e., $\sim 02:07$ UT ± 16 minutes adding the light travel time). The long path length inferred by this method ($D = 1.83 \pm 0.22$ au for *STEREO-B*, $D = 1.37 \pm 0.16$ au for *STEREO-A*, and $D = 3.99 \pm 0.49$ au for *SOHO*) may result from either a non-standard IMF topology (longer than the expected length of the nominal Parker spiral IMF lines), a delay in the low-energy proton injection with respect to high energies, or that the particles experienced energy-dependent scattering processes on their path from the Sun to each spacecraft (e.g., Laitinen et al. 2015a). We have also applied the same least-squares fitting to the *Wind*/3DP/SST electron onsets and obtained a release time of $A = 117 \pm 33$ minutes (i.e., $\sim 02:05$ UT ± 33 minutes adding the light travel time), and a path length $D = 4.03 \pm 2.3$ au. The long distances inferred for L1 observers may be due to not only an energy dependence of injection and transport of the particles but also to the presence of the prior CME (Figure 2(c)) that might have distorted the nominal transport conditions between the Sun and Earth.

4.2. The SEP Event at 0.40 au

Figure 12 shows, from top to bottom, (a) near-relativistic electron intensities measured in two different energy channels of *MESSENGER*/EPS, and the magnetic field (b) magnitude, (c) polar and (d) azimuth angles in the spacecraft-centered RTN coordinate system as measured by the magnetometer (MAG)

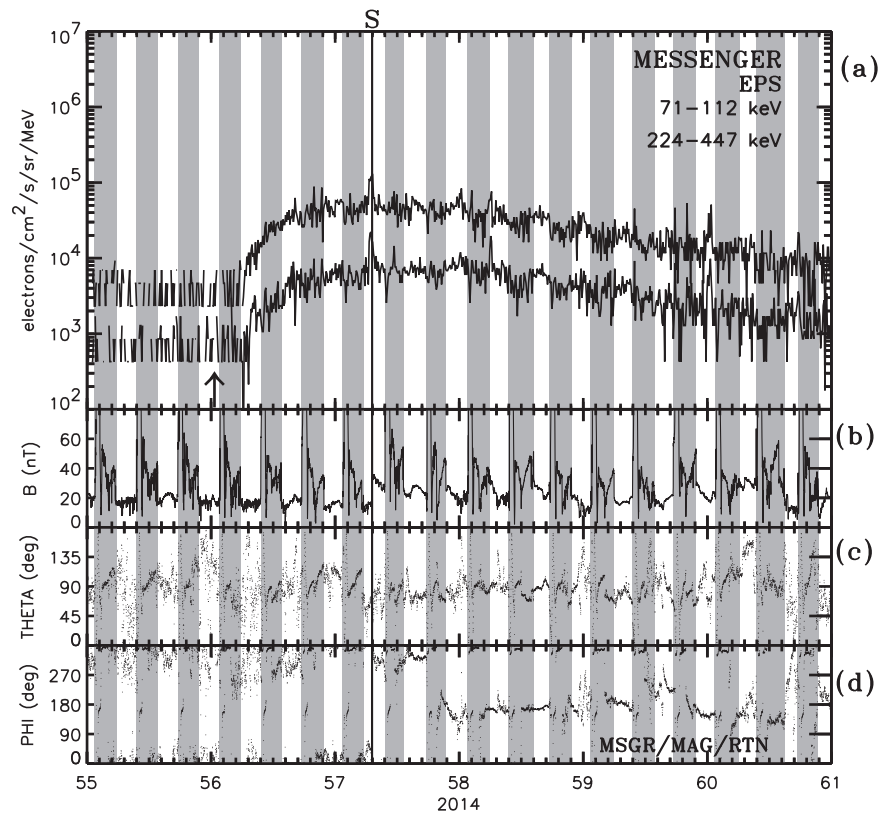


Figure 12. *MESSENGER* observations: (a) electron intensities at two energy channels, (b) magnetic field magnitude, and (c)–(d) magnetic field angular direction in the RTN coordinate system. The vertical gray bars identify time intervals when the spacecraft transited Mercury’s magnetosphere, and the solid vertical line identifies the passage of an interplanetary shock.

onboard *MESSENGER* (Anderson et al. 2007) from day 55 to day 61 of 2014. The onset of the SEP event at *MESSENGER* was observed in the 71–112 keV electron channel at $\sim 06:50$ UT on day 56. Considering the field of view of EPS (pointing mostly in the antisunward direction, cf. Andrews et al. 2007), the elevated instrumental background (cf. Figure 1 in Lario et al. 2013), and assuming that EPS responds mostly to electrons of the indicated energy, we estimate an upper limit for the release of the electrons observed by *MESSENGER* at $\sim 06:53$ UT by assuming scatter-free propagation along the nominal Parker spiral IMF connecting the Sun to *MESSENGER* ($L_{MSGR} \sim 0.41$ au) (with the travel light time to 1 au already added). The arrival of particles to be observed by *MESSENGER*/EPS field of view requires particles to be directed toward the Sun by either scattering or mirroring processes in the interplanetary medium and hence that the estimated release time should only be considered as an upper limit (i.e., it may occur before 06:53 UT).

Periodic increases in the magnetic field magnitude shown in Figure 12(b) are due to the *MESSENGER*’s orbit about Mercury and the close proximity of the spacecraft to the planet at each periapsis. The vertical gray bars identify time intervals when *MESSENGER* transited Mercury’s magnetosheath and magnetosphere; the start and end times of each vertical gray bar mark the inbound and outbound crossings of *MESSENGER* through Mercury’s bow shock (cf. Winslow et al. 2013). The periods between the gray vertical bars in Figure 12 indicate that the spacecraft was immersed in the solar wind and are the intervals of interest here. The black solid vertical line labelled with the letter S indicates the passage of an

interplanetary shock at 57/07:09 UT identified by an abrupt increase in magnetic field magnitude (this shock passage has been identified with the vertical purple line in Figure 1(d)). By assuming that this shock originated at the Sun at the time of the X4.9 flare (00:39 UT), we infer an average transit speed of ~ 545 km s $^{-1}$. We do not see any clear signature of an ICME following this shock during the intervals when *MESSENGER* was in the solar wind. Assuming that the shock was centered at the longitude of the X4.9 flare, the observation of the shock by *MESSENGER* implies a minimum width of $\sim 113^\circ$ (or by symmetry of $\sim 226^\circ$) when it arrived at 0.40 au. Magnetic field observations allow us to estimate the magnetic field compression ratio across of the shock of $r_B \sim 1.90$.

4.3. The SEP Event at 2.11 au

Figure 13(a) shows charged particle intensities measured by the electron solid state detector (SSD) of the A180 sensor of the JEDI experiment on board *Juno* (Mauk et al. 2013). The A180 sensor has a field of view of 160° (with a 12° blockage) covering from sunward to anti-sunward directions (cf. Figures 15 and 16 in Mauk et al. 2013). Comparisons performed on other events between the responses of the electron SSD and the ion SSD of the A180 sensor (Figure 45 in Mauk et al. 2013) show that the early part of the event is primarily electrons whereas the later part of the event may contain substantial contributions from >250 keV protons, mainly at the arrival of the shock (indicated by the solid vertical line in Figure 13). In order to match *MESSENGER* energy channels, we have added

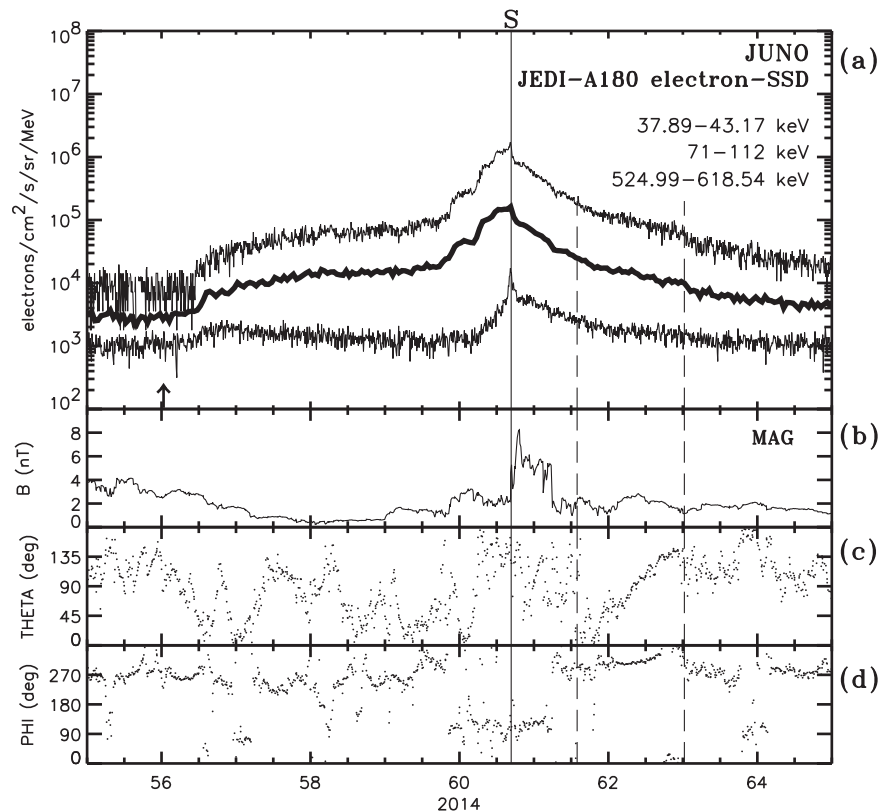


Figure 13. *Juno* observations: (a) electron intensities in three different energy channels, (b) magnetic field magnitude, and (c)–(d) magnetic field angular direction in the RTN coordinate system. The solid vertical line identifies the passage of the interplanetary shock and the dashed vertical lines the passage of an ICME identified by the smooth rotation of the magnetic field.

in Figure 13(a) 71–112 keV electron intensities inferred from the energy spectra formed from the electron energy channels of JEDI/A180 (thick black trace). Particle intensities at *Juno* did not increase until $\sim 10:15$ UT on day 56. Assuming scatter-free propagation along the nominal Parker IMF line of $L_{Juno} \sim 3.28$ au we infer an upper limit for the release of 525–618 keV electrons at 09:52 UT (where we have already added the transit light time to 1 au to compare with the solar electromagnetic emissions described in Section 3).

The three bottom panels of Figure 13 show the magnetic field magnitude and angular orientation in the RTN spacecraft centered coordinate system as observed by the magnetic field investigation onboard *Juno* (Connerney et al. 2013). Based uniquely on the magnetic field data, we see that the passage of a shock at 60/16:39 UT (indicated by the solid vertical line labelled S) was followed by the rotation of the magnetic field suggesting the passage of a magnetic cloud starting at $\sim 13:50$ UT on day 61 and ending at $\sim 00:25$ UT on day 63 (indicated by the vertical dashed lines in Figure 13). By assuming that this shock originated at the Sun at the time of the X4.9 flare (00:39 UT on day 56), we infer an average transit speed of ~ 783 km s $^{-1}$ and a minimum width of $\sim 34^\circ$ assuming that it was centered on the flare site (or 68° assuming symmetry about the flare site). The fact that the magnetic field rotation was not observed by any of the other spacecraft analyzed in this paper, implies that the width of the flux rope behind the shock extended a minimum of $\sim 68^\circ$ but did not reach $\sim 156^\circ$, since it was not observed by *STEREO-B* or *ACE*. Magnetic field observations allow us to estimate the magnetic field compression ratio across the shock of $r_B \sim 2.77$.

5. EVIDENCE FOR AN EXTENDED INTERPLANETARY SHOCK

The solar eruption early on 2014 February 25 generated a global SEP event observed by spacecraft distributed through the inner heliosphere. The in situ observation of an interplanetary shock by the selected spacecraft (indicated by the purple vertical lines in Figures 1(b)–(f) and by the letter S in Figures 9, 12, and 13) opens the possibility to determine the longitudinal extent of the shock. Assumptions that this shock originated at the Sun at the time of the X4.9 flare and that it was symmetric about the longitude of the solar flare imply that the shock had a minimum width of $\sim 226^\circ$ when it passed by 0.4 au and of $\sim 164^\circ$ when it passed by L1. The observation of the shock by *STEREO-B* implies a width of $\sim 156^\circ$ if symmetric around the flare site. If *STEREO-A* observed the same shock, we can extend the longitude span of the shock at ~ 1 au up to $\sim 250^\circ$ (again assuming symmetry about the flare site). Of course, the occurrence of CMEs before and after the onset of the SEP event complicates the association between the shock observed by each one of the five spacecraft and its solar source. According to the CME LASCO catalog at cdaw.gsfc.nasa.gov/CME_list/, no CMEs sufficiently fast to explain the origin of the shock S at the five spacecraft occurred after the X4.9 flare. Therefore, we analyze the possibility that the shock S could have been associated with a CME occurring prior to the onset of the SEP event.

Table 2 lists the CMEs observed by *SOHO*/LASCO with widths $>80^\circ$ and plane-of-sky speeds >450 km s $^{-1}$ for four days prior to the onset of the SEP event (as listed in the CME LASCO catalog posted on cdaw.gsfc.nasa.gov/CME_list/).

Table 2
CMEs Observed by *SOHO*/LASCO Prior to the Onset of the SEP Event on 2014 February 25^a

LASCO Time ^b (day/hour) (1)	CME PA ^c (deg) (2)	Plane-of-sky Width (deg) (3)	CME Speed (km s ⁻¹) (4)	EUVI Time (day/hour) (5)	Eruption Site ^d (6)	<i>STEREO-A</i> $\langle V_{\text{shock}} \rangle^e$ (km s ⁻¹) (7)	<i>STEREO-B</i> $\langle V_{\text{shock}} \rangle^e$ (km s ⁻¹) (8)	L1 $\langle V_{\text{shock}} \rangle^e$ (km s ⁻¹) (9)	<i>MESSENGER</i> $\langle V_{\text{shock}} \rangle^e$ (km s ⁻¹) (10)
52/16:00	Halo	360	1252	52/15:31	S15E120	267	283	284	149
53/12:12	247	233	1023	53/~09:45	S27-34W141-175 ^f	304	321	325	178
53/15:48	096	160	0696	53/15:31	S10E100	318	335	341	190
54/06:48	114	084	0540	54/06:17	S15E105	361	377	388	228
54/06:48	262	162	0770	54/06:16	S16W109	361	376	388	228
55/11:36	094	193	0495	55/11:11	S14E90	489	498	534	379
55/23:24	267	188	0790	55/23:01	S19W128	568	575	632	519
56/01:25	Halo	360	2147	56/00:39	S12E82	585	587	648	545

Notes.

^a Only CMEs with widths $>80^\circ$ and speed $>450 \text{ km s}^{-1}$ as reported in the LASCO CME catalog at cdaw.gsfc.nasa.gov/CME_list/.

^b Time of the first appearance in the C2 coronagraph. The date is given in day of the year 2014 and time in UT.

^c Position angle (PA) measured from Solar North in degrees (counter-clockwise).

^d Heliographic latitude and longitude as seen from Earth and identified using 5-minute cadence SECCHI/EUVI 195 Å images.

^e Estimated shock average transit speed assuming that the shock S in Figures 9 and 12 at *STEREO-A*, *STEREO-B*, L1 and *MESSENGER* was associated with this CME.

^f Site of a large filament eruption associated with the origin of the CME.

Using EUV observations from *STEREO*/SECCHI/EUVI, we have identified the time (within the 5 minute cadence of the instrument images) and site of the solar eruption origin of these CMEs (listed in columns 5 and 6 of Table 2). Columns 7–10 of Table 2 show the average transit speed resulting from the association of the shock observed by *STEREO-A* at 58/20:47 UT, *STEREO-B* at 59/04:24 UT, L1 at 58/16:08 UT and *MESSENGER* at 57/07:04 UT originated at the time of each one of the CMEs listed in Table 2.

1. Given the longitudes of the solar eruptions listed in column 6 of Table 2 (all of them more distant from the Sun–Earth line than the CME early on day 56) and the strength of the shock observed at L1 (cf. Figure 9), the most likely origin of the shock S at Earth was the west flank of the shock driven by the CME early on day 56 with an average transit speed of 648 km s^{-1} resulting in a shock width of at least 82° westward of the flare site.
2. Out of the CMEs in Table 2, those propagating toward western longitudes (as seen from Earth; i.e., position angles (PA) around $\sim 270^\circ$) and generated by eruptions at western longitudes would facilitate the observation of a shock at *MESSENGER*. However, the CME at 54/06:48 UT gives only an average transit speed of $\sim 228 \text{ km s}^{-1}$ unlikely to produce a strong shock at *MESSENGER*. The CME at 55/23:24 UT yields an average transit speed of 519 km s^{-1} , but the width of this CME inferred from the white-light coronagraph images (Section 3) is not enough to reach *MESSENGER*. Therefore, we believe that the shock at this spacecraft originated at the Sun in association with the CME early on day 56 (and therefore the shock had at least a minimum width of 113° westward of the flare site). If the shock was symmetric around the flare site, its longitudinal extent when arriving at 0.4 au would have been 226° .
3. The strong shock observed by *STEREO-B* (Figure 9) would be favored if its origin was associated with an eastern solar eruption (as seen from Earth). The characteristics of the shock contrast with the low average

transit speeds listed in Table 2 computed for the CMEs originated from longitudes eastward of E82. Therefore, we believe that the origin of the shock at *STEREO-B* was associated with the CME early on day 56 (and therefore the shock had a minimum width of 78° eastward of the flare site, assuming that it originated at the X4.9 flare site).

4. If the shock at *STEREO-A* originated from one of the east-directed CMEs, we would expect a stronger shock at *STEREO-B* than at *STEREO-A* (as observed, cf. Figure 9). However, the association made between the shock at *STEREO-B* and the CME early on day 56, together with the fact that no clear shock was observed by this spacecraft before day 59, implies that the shock at *STEREO-A*, if coming from an eastern longitude, originated at the time of the CME early on day 56. The CME at 53/12:12 UT was generated by a filament eruption very close to the Sun–*STEREO-A* line, and therefore it is a good candidate for the origin of the shock S at *STEREO-A*. However, its low average transit speed contrasts with the elevated coronagraph plane-of-sky speed of this CME. Therefore, we suggest that the CME at 53/12:12 UT might be a good candidate for the shock and ICME observed in situ by *STEREO-A* on day 56 (Figure 9) implying an average transit speed for the shock of $\sim 533 \text{ km s}^{-1}$, but not for the shock S. If the shock S at *STEREO-A* was generated from a western-directed CME, and the shocks at *STEREO-A* and *STEREO-B* had a common origin, the shock at *STEREO-A* would have been stronger than at *STEREO-B* which is not observed. Therefore, if the shock S at *STEREO-A* originated in a western-directed CME, it would have had a different origin than the shock at *STEREO-B*. There exists the possibility that the shock S at *STEREO-A* was indeed a flank of the shock originated at the time of the western-directed CME at 55/23:24 UT. The width of this CME inferred from the white-light coronagraph images (Section 3) allows for the possibility that a weak flank of the associated shock glanced *STEREO-A*. Note that the

observation of ICME signatures by *STEREO-A* after the passage of the shock S (www-ssc.igpp.ucla.edu/forms/stereo/stereo_level_3.html) would favor this different origin of the shock observed by this spacecraft, although the evidence of an ICME at *STEREO-A* (only based on intermittent bidirectional suprathermal electrons) is not particularly strong.

- Given the longitude separation between *Juno* and the flare X4.9 site ($\Delta\phi = 34^\circ$) together with the computed average transit speed ($\sim 783 \text{ km s}^{-1}$), we believe that the shock observed by this spacecraft was indeed the shock generated by the CME early on day 56.

Therefore, we conclude that the shock S observed by *Juno*, *MESSENGER*, L1 and *STEREO-B* originated by the CME early on day 56, whereas the origin of the shock at *STEREO-A* is uncertain. The observation of the shock by *MESSENGER* implies a minimum width of $\sim 113^\circ$ westward of the flare site. The observation of the shock by *STEREO-B* implies a shock width of $\sim 78^\circ$ eastward of the flare. Therefore, the shock S was at least $\sim 191^\circ$ wide (i.e., 113° westward plus 78° eastward of the flare). If the shock S at *STEREO-A* originated by the same event, it extended $\sim 125^\circ$ eastward of the flare site, implying a shock span of at least $\sim 238^\circ$ (i.e., $113^\circ + 125^\circ$). Note that if instead of using the flare longitude (E82) we use the longitudinal direction of the nose of the shock front provided by the fitted ellipsoid (i.e., E91 when the leading edge of the shock front was already at $12.7 R_\odot$ from the shock surface, see Section 3), the IP shock had a minimum width of 122° westward of its nose direction (as seen by *MESSENGER*) and 69° eastward of the nose direction (as seen by *STEREO-B*); giving a total width of at least 191° . If *STEREO-A* observed the same shock we infer then a width of 116° eastward of the nose of the fitted shock (and by symmetry 232°).

Under the assumption that the shock S at the different spacecraft had a common origin, we plot in Figure 14(a) the averaged transit speed of the shock to travel from the Sun to each spacecraft (V_{shock}) as a function of the longitudinal distance $\Delta\phi$ between the flare site and the heliolongitude of each spacecraft ($\Delta\phi = -34^\circ$ for *Juno* (green symbol), -82° for L1 (black symbol), -113° for *MESSENGER* (orange symbol), $+78^\circ$ for *STEREO-B* (blue symbol), and $+125^\circ$ for *STEREO-A* (red symbol)). Assuming that the shock speed follows a longitudinal dependence as $V(\Delta\phi) = V_0 \cos(\Delta\phi) + V_1$ (as suggested by Smart & Shea 1985) we obtain the least-square fit indicated by the solid curves in Figure 14(a). The purple line is obtained assuming that the shock at *STEREO-A* had the same origin, whereas the gray line does not consider the observation from *STEREO-A*. Figure 14(a) shows that the shock was faster in the direction of *Juno* because of its longitudinal proximity to the flare site, whereas the transit speeds decrease very fast with longitude. The ICME following the passage of the interplanetary shock was only detected by *Juno*, i.e., the spacecraft closest in longitude to the flare site (cf. Figure 1). Therefore, Figure 14(a) shows that the transit speed observations are not consistent with a spherical IP shock propagating at a constant speed (as shown for example by Smith & Dryer 1990).

Figure 14(b) shows the longitudinal dependence of the magnetic field compression ratio r_B at the time of the shock passage by each spacecraft (using the same color code). The two curves are least-squares fits of a functional form as $r_B(\Delta\phi) = r_0 \cos(\Delta\phi) + r_1$ to all five data points (purple line)

and without considering the *STEREO-A* data point (gray line). The functional form assumes that the shock was stronger near its nose (centered at the longitude of the flare site) and weaker at its flanks. Note that the different radial distance of *Juno* and *MESSENGER* may play a role in the observed values of r_B as well as the fact that r_B responds to a local measure of the shock.

6. LONGITUDINAL AND RADIAL DEPENDENCES OF SEP PEAK INTENSITIES

Figure 1 shows that the shapes of the SEP intensity-time profiles were ordered in terms of the heliolongitude of the observer with respect to the site of the parent solar event. Whereas the SEP intensity at both *STEREOs* were dominated by the first peak observed shortly after the onset of the event, for spacecraft at L1 the peak intensity occurred after the shock passage. For observers at ~ 1 au, the peak intensities during the prompt component of the event were larger at *STEREO-B*, followed by *STEREO-A* and then at L1 observers (Figure 8). Figure 14(c) shows the 71–112 keV electron peak intensity at the prompt component of the event as a function of the longitudinal separation between the nominal Parker IMF footpoints and the flare site $\Delta\psi$ (we have removed the pre-event background intensity, applied the intercalibration factor between *ACE/EPAM/DE* and *STEREO/SEPT* electron intensities described in Figure 2 of Lario et al. (2013), and assume that *MESSENGER* and *Juno* data do not need any factor of calibration). The purple line in Figure 14(c) is a Gaussian function $j(\Delta\psi) = j_0 \exp\{-(\Delta\psi - \phi_0)^2/2\sigma^2\}$ passing over the three observations at ~ 1 au. The observations at distances different from 1 au (orange symbol for *MESSENGER* and green symbol for *Juno*) include also radial intensity gradients and therefore are not considered in the Gaussian fit.

Figures 1 and 9 show that at the time of the passage of the shock S by each spacecraft, the largest electron intensities at ~ 1 au were observed at L1, followed by *STEREO-B* and very low values were observed by *STEREO-A*. The same trend is observed for proton intensities (Figures 1 and 8(a)). For wide CME-driven shocks generated from eastern longitudes, the peak intensity tends to be observed after the shock passage (this is the case for L1 observers); whereas for western events (such as the case of *STEREO-A* and *STEREO-B* in this event) the intensities already decrease at the time of the shock passage by the spacecraft location, if the shock is observed at all (e.g., Lario & Simnett 2004). The short duration of the event at *STEREO-A* in comparison with the event at *STEREO-B* may respond to the time interval that each spacecraft remains connected to the region of the traveling CME-driven shock that is able to inject particles. Both *STEREOs* were connected to strong portions of the shock front when the shock was still close to the Sun, but as the shock expanded into IP space they established magnetic connection to the weak flank of the shock, with *STEREO-A* being the first spacecraft to lose its connection to the region of the shock able to accelerate energetic particles. By contrast, L1 observers established magnetic connection to the strongest portions of the shock as the shock expanded into interplanetary space and hence the different time profiles shown in Figure 8 (Cane et al. 1988).

Figure 14(d) shows the 71–112 keV electron intensities at the time of the shock passage as a function of the longitudinal distance $\Delta\phi$ between the flare site and the heliolongitude of each spacecraft (no pre-event intensities have been subtracted). In principle, the shock should be stronger near its nose that

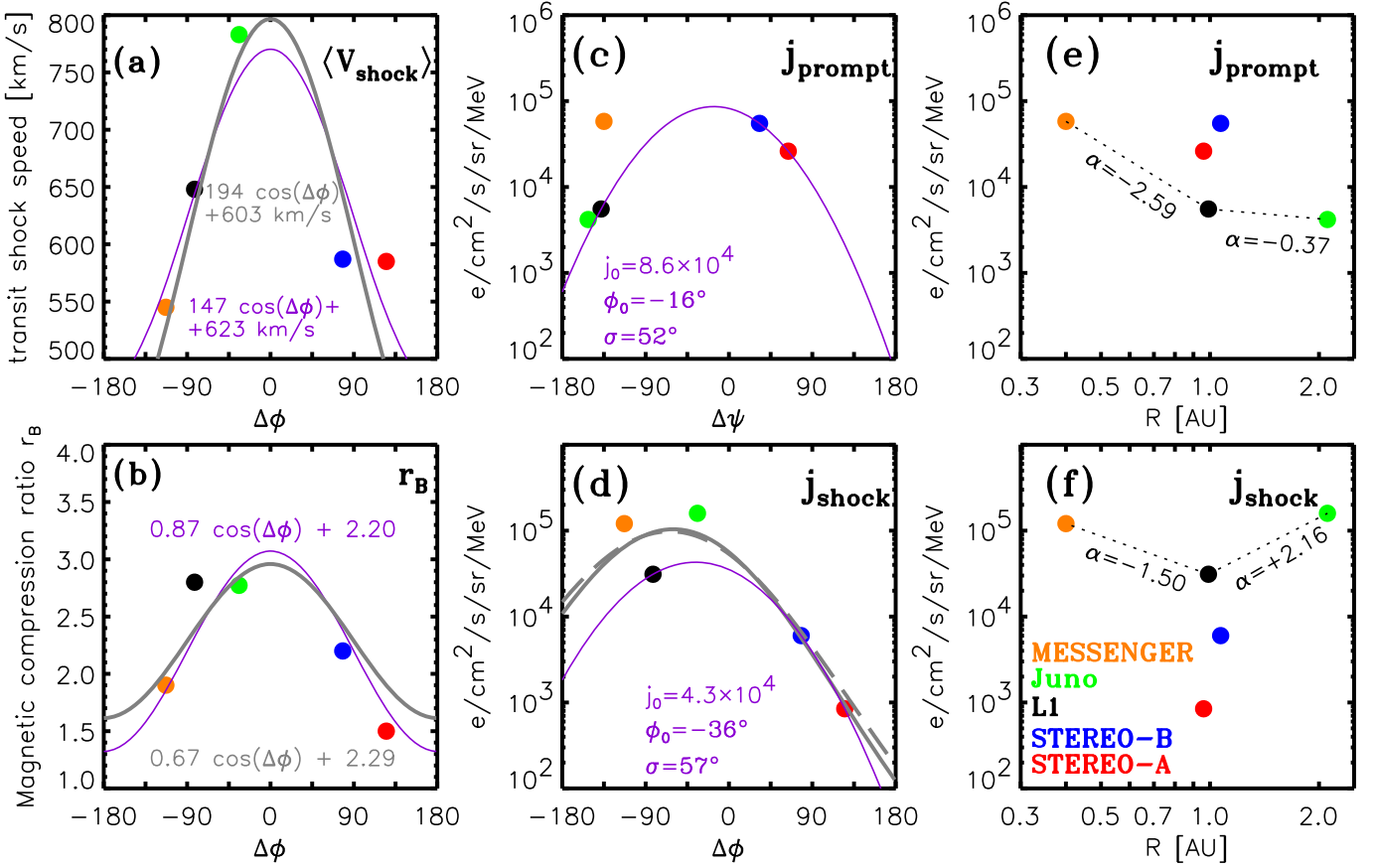


Figure 14. (a) Longitudinal dependence of the average transit shock speed. Red, blue, black, orange, and green symbols indicate *STEREO-A*, *STEREO-B*, L1, *MESSENGER*, and *Juno*, respectively. The solid curves are least-square fits assuming a dependence $\propto V_0 \cos \Delta\phi + V_1$ to all data points (purple line) and to the data points but excluding *STEREO-A* (gray line). (b) Longitudinal dependence of the shock magnetic compression ratio r_B . The curves are least-square fits assuming a dependence $\propto r_0 \cos \Delta\phi + r_1$ to all data points (purple line) and to the data points but excluding *STEREO-A* (gray line). (c) 71–112 keV electron peak intensity measured at the prompt component of the event (j_{prompt}) as a function of the longitudinal distance between the nominal footpoint of the spacecraft and the flare site. The purple line is a Gaussian fit to the ~ 1 -au data points. (d) 71–112 keV electron peak intensity measured at the shock passage (j_{shock}) as a function of the longitudinal distance between spacecraft location and flare site $\Delta\phi$. The purple line is a Gaussian fit to data points at ~ 1 au, whereas the gray lines consider all data points (solid gray line) and all the data points but excluding *STEREO-A* (dashed gray line). (e) Radial dependence of the 71–112 keV electron peak intensity measured at the prompt component of the event. (f) Radial dependence of the 71–112 keV electron peak intensity measured at the passage of the shock. The dotted straight lines in panels (e) and (f) assume a radial dependence as $\propto R^{-\alpha}$ for those spacecraft closely connected with L1.

would have been located around the flare longitude. The purple line in Figure 14(d) is a Gaussian fit to 1-au observations, whereas the gray line is a Gaussian fit to all five data points (the gray dashed line is the same fit without considered the *STEREO-A* data point). Since *Juno* and *MESSENGER* data points are taken at different helioradii, they include possible radial dependence of particle acceleration mechanisms as the shock propagated away from the Sun. Although the values of $|\Delta\phi|$ for L1 and *STEREO-B* were similar, particle intensities at the shock passage were higher at L1 than at *STEREO-B*, especially for high-energy proton and ion, as well as for electron intensities (cf. Figure 1). This phenomenon has been usually interpreted as an east–west asymmetry in the particle enhancements associated with the passage of CME-driven shocks due to the large-scale structure of the shock and its capability to accelerate electrons and protons to high energies (i.e., quasi-perpendicular versus quasi-parallel geometries depending on whether the parent solar eruption occurs from eastern or western longitudes from the point of view of the observer, see Sarris & Krimigis 1985 and Figure 6 in Zank et al. 2006). In fact the angle between the normal to the shock and the upstream magnetic field was $\theta_{Bn} \sim 83^\circ$ for *ACE* (as

reported in www.cfa.harvard.edu/shocks and $\theta_{Bn} \sim 54^\circ$ for *STEREO-B* (as reported in `ipshocks.fi` and computed using the same method MD3 (from Abraham-Shrauner & Yun 1976) in both cases). Nevertheless, we should also indicate that (i) the shock at L1 was stronger than at *STEREO-B* (Figures 9(b) and (f)) and, in principle, more capable of accelerating particles to high-energies (Lario et al. 2005; Giacalone 2012), and (ii) shock parameters are based on a local measure of the shock whereas particle intensities depend on the whole time history of the event.

Figures 14(e) and (f) show the radial dependence of the 71–112 keV electron peak intensities at the prompt component (14e) and at the shock passage (14f). For those spacecraft with close magnetic connection (L1, *MESSENGER* and *Juno*; cf. Figure 1), we have assumed a radial dependence $\propto R^{-\alpha}$ (indicated by the dotted lines). The decrease of particle intensities from 0.40 to 1.0 au is consistent with radial dependences obtained in prior studies (e.g., Lario et al. 2006, 2007, 2013). However, the similar intensities observed by L1 and *Juno* at the prompt component of the event together with the higher intensities measured at *Juno* with respect to Earth at the time of the shock do not follow the expected radial

Table 3
Shock Height at the Particle Release Times

Particle Species/Spacecraft/Instrument	Estimated Release Time (UT) ^a	Shock Height Above Sun Surface ^b	θ_{Bn} at the Cobpoint ^c
(1)	(2)	(3)	(4)
Protons/ <i>STEREO-B</i> /HET (13–100 MeV)	00:57 ± 7 minutes (VDA)	2.3 ± 1.0 R_{\odot}	55° ± 24°
60–100 MeV Protons/ <i>STEREO-B</i> /HET	01:07 ± 2 minutes (TSA)	4.0 ± 1.0 R_{\odot}	29° ± 5°
375–425 keV Electrons/ <i>STEREO-B</i> /SEPT	01:07 ± 2 minutes (TSA)	4.0 ± 1.0 R_{\odot}	29° ± 5°
0.7–1.4 MeV Electrons/ <i>STEREO-B</i> /HET	01:07 ± 2 minutes (TSA)	4.0 ± 1.0 R_{\odot}	29° ± 5°
Protons/ <i>STEREO-A</i> /HET (13–100 MeV)	01:05 ± 6 minutes (VDA)	1.9 ± 1.5 R_{\odot}	59° ± 16°
60–100 MeV Protons/ <i>STEREO-A</i> /HET	01:07 ± 2 minutes (TSA)	2.2 ± 0.8 R_{\odot}	56° ± 10°
375–425 keV Electrons/ <i>STEREO-A</i> /SEPT	01:03 ± 3 minutes (TSA)	1.4 ± 0.9 R_{\odot}	63° ± 11°
0.7–1.4 MeV Electrons/ <i>STEREO-A</i> /HET	01:07 ± 2 minutes (TSA)	2.2 ± 0.8 R_{\odot}	56° ± 10°
Protons/ <i>SOHO</i> /ERNE (13.8–101 MeV)	02:07 ± 16 minutes (VDA)	>2.3 (1.4,2.5) ^d R_{\odot}	<29°
Protons/ <i>SOHO</i> /ERNE (80.2–101 MeV)	03:06 ± 2 minutes (TSA)	>3.7 (3.4,4.2) ^d R_{\odot}	<26°
Near-relativistic Electrons/ <i>Wind</i> /3DP (39–303 keV)	02:05 ± 33 minutes (VDA)	>0.8 (<1.4, 3.0) ^d R_{\odot}	<32°
175–315 keV Electrons/ <i>ACE</i> /EPAM/DE	02:32 ± 2 minutes (TSA)	>3.7 (2.5, 3.0) ^d R_{\odot}	<26°
0.25–0.70 MeV Electrons/ <i>SOHO</i> /EPHIN	02:10 ± 2 minutes (TSA)	>3.7 (1.5, 2.1) ^d R_{\odot}	<26°
71–112 keV Electrons/ <i>MESSENGER</i> /EPPS	<06:53 ± 10 minutes (TSA)	≫3.7 R_{\odot}	≪26°
525–618 keV Electrons/ <i>Juno</i> /JEDI	<09:52 ± 10 minutes (TSA)	≫3.7 R_{\odot}	≪26°

Notes.

^a Light travel time already added. The method used to estimate the particle release time is indicated by VDA for velocity dispersion analysis and TSA for time-shifted along the nominal Parker spiral length.

^b Shock height estimated at the cobpoint of each spacecraft using the PFSS field line approach. The range of heights includes the uncertainty in the estimated SEP release time.

^c Angle between the normal to the shock and the magnetic field direction at the cobpoint (estimated using the PFSS + Parker spiral method).

^d Values of the L1 cobpoint heights listed between parentheses are estimated using the portion of the white-light shock moving over the west limb (as seen from Earth) in the plane-of-sky images taken by *SOHO*/LASCO/C2, rather than using the ellipsoid fit. The height of the cobpoint at the estimated SEP release time is included within the range of distances indicated between parentheses.

dependences where particle intensities and weakening of shock efficiency in particle acceleration are supposed to decrease with radial distance. Intercalibration and energetic proton contamination of electron measurements may contribute to this latter inconsistency.

7. CME-DRIVEN SHOCK LOCATION AT THE SEP RELEASE TIMES

The tracking of the shock front at different times (Section 3) allows us to estimate its location at the times we inferred for the release of SEPs. Table 3 lists the estimated SEP release times using either the VDA method shown in Figure 11 or, for some specific energy channels, a time-shifted analysis (TSA) that assumes scatter-free propagation of particles along nominal Parker spiral IMF lines of length L inferred from the solar wind speed measured at the onset of the SEP event (column 7 in Table 1). Whereas the different methods give similar values for the release of particles observed by *STEREO-A*, for *STEREO-B* there is a difference of ~10 minutes between the release times obtained by the VDA and the TSA methods. Energy dependent scattering processes may contribute to the earlier estimation provided by the VDA method (e.g., Laitinen et al. 2015a). By contrast, the estimated release times of the particles observed at L1 provided by the different methods may differ by up to ~1 hr. Clearly, the assumptions of scatter-free transport, simultaneous release of particles propagating along a common path-length, or that the path length is given by a nominal Parker spiral IMF line are not accurate representations of the actual

conditions for the arrival of particles at L1. Note also that there is a significant delay between the estimated release times of the SEPs observed at the different spacecraft and the onset (00:39 UT) and peak (00:49 UT) of the associated SXR flare emission.

In order to compute the height of the shock at the time of the release of the particles observed by each spacecraft, we have considered the point of intersection between the field lines plotted in the fourth column of Figure 6 with the modeled front shock (i.e., the “cobpoint” after Heras et al. 1995). Column 3 of Table 3 lists the height of the cobpoint of each observer above the solar surface for the times listed in column 2. The errors associated with the cobpoint heights are such that the range of radial distances covers the complete range of estimated release times within the error bars.

For the release time of particles observed at L1 we list two sets of values for the cobpoint height. The first set of numbers in column 3 of Table 3 are lower limits of the L1 cobpoint height obtained from the ellipsoid fitting. Because of the field of view of the *STEREO* coronagraphs, the tracking of the shock with the ellipsoid has only been done below 15 R_{\odot} . For the range of release times listed in column 2 of Table 3 for L1, the leading edge of the ellipsoid was already outside this domain, the last image with the complete ellipsoid within the observed images being made at 01:53 UT when the L1 cobpoint was at height of 3.7 R_{\odot} . Therefore, we list a lower boundary for the height of the cobpoint, obtained at the earliest time that is within the error in the release time. The pair of L1 cobpoint heights between parentheses in column 3 of Table 3 corresponds to the range of heights of the portion of the white-light

shock moving over the west limb (as seen from Earth) estimated from plane-of-sky images taken by *SOHO*/LASCO/C2 (such as those of Figure 7). This range of heights cover the radial distances of the plane-of-sky shock during the time interval of estimated particle release times.

Although the longitudinal separation between *STEREO-A* and *STEREO-B* was 47° , the release of the first particles arriving at *STEREO-A* and *STEREO-B* occurred at similar times. It is interesting to note that the estimated footpoints of both spacecraft using the PFSS and MAS models are very close to each other, with a difference in longitude of only $\sim 4^\circ$ (Table 1). Because of the divergence of the field lines connecting to *STEREO-A* and *STEREO-B* (Figure 6(d)), at the time of the particle release, the height of the *STEREO-B* cobpoint was higher than that of *STEREO-A*. The particles observed by both spacecraft were released when the portion of the shock connecting to each observer was already at some distance ($\gtrsim 2 R_\odot$) above the solar surface.

The field of view and elevated instrumental background of *MESSENGER*/EPS only provides us an upper limit for the release of particles observed at 0.40 au. Similarly, the large heliocentric distance of *Juno* limits our estimation of the release time of particles observed at 2.11 au and the height of the shock at that time.

Finally, column 4 of Table 3 lists the range of angles formed between the normal to the ellipsoid and the IMF field line connecting to each observer (considering the PFSS approximation if the cobpoint is below $2.5 R_\odot$ and the Parker spiral field line if the cobpoint is above $2.5 R_\odot$). Because of the structure of the shock and the topology of the field lines (Figure 6(d)), at the release time of the particles observed by *STEREO-A* the shock was mostly quasi-perpendicular. For *STEREO-B* and for the particle release times estimated by the TSA method, the shock was mostly quasi-parallel. The global shock fitted by the ellipsoid evolved to quasi-parallel as it expanded away from the Sun. The estimation of θ_{bn} for L1 observers is not completely resolved because of the uncertainties on the white-light shock fitting at these longitudes (Figure 6). However, the large heights of the shock at these release times suggest that the shock was mostly quasi-parallel.

The Fe enhancement observed at high energies early in the event by all three spacecraft at ~ 1 au (Figure 8(c)) is at odds with the proposal that the shock parameters at the corona determine the ion composition properties of the SEP events (Tylka et al. 2005). Our approach shows that at the estimated release times of the particles, the shock was mostly quasi-parallel at the region connected to *STEREO-B* and L1 observers, more quasi-perpendicular for *STEREO-A*, and evolved to quasi-parallel as it expanded away from the Sun. Nevertheless, all three spacecraft detected high-energy Fe-rich prompt components (Figure 8(c)). It is possible that the Fe enhancement observed at high energies at all three locations was due to a Fe-rich seed population already present in the medium from prior events that was re-accelerated by the shock regardless of the shock parameters and of the region of the shock connecting to each spacecraft. If Fe-rich intensities at the three spacecraft were solely due to an intense contribution of particles accelerated at the site of the X4.9 flare, strong diffusion processes would be needed to explain their arrival at the *STEREOs* and L1 spacecraft.

8. SUMMARY

The multi-spacecraft SEP event on 2014 February 25 was generated by a single eruption that originated from the NOAA active region 11990 at S12E82. The site of this eruption was well separated from the estimated magnetic footprint locations of all the spacecraft in the interplanetary medium that detected SEPs (Figure 1). Although the EUV signatures associated with the eruption of this event were very limited in longitude (cf. Long et al. 2015, and Figure 5), a SEP event with fast rising intensities and rich in Fe ions (Figure 8) was observed even at distant longitudes from the event. Therefore, the extent of the EUV wave over the solar disk does not indicate the extent of the SEP event in interplanetary space.

The origin of the SEP event observed at different longitudes was an asymmetric CME that eventually reached the category of halo CME (umbra.nascom.nasa.gov/lasco/observations/halo/) as seen from L1 by *SOHO* coronagraphs (cdaw.gsfc.nasa.gov/CME_list) and from both *STEREO* spacecraft (cor1.gsfc.nasa.gov/catalog/). Because of the effects that coronal streamers produce on the propagation of CMEs, the outermost front of the CME did not propagate symmetrically around the Sun but mostly toward eastern longitudes as seen from Earth. Kwon et al. (2015) suggested that the halo shaped front observed around the Sun is not the projection of an expanding ejecta traveling in a direction lying near the line of sight, but is due to the projection of a spherically expanding fast magnetosonic shock wave enclosing the Sun. With the uncertainty of the portion of the shock propagating over western longitudes (as seen from Earth), the geometric shape used to fit EUV and white-light coronagraph observations provides a shock front that eventually covered the whole Sun (Figure 6). Whereas a shock wave close to the Sun may expand over a wide range of heliolongitudes, as it propagates into IP space, only those portions driven by the CME are strong enough to be observed by spacecraft located at a certain distant helioradius. Therefore, in general, stronger and faster shocks should be observed by spacecraft at small longitudinal distances from the CME propagation direction (Figures 14(a), (b)). By contrast, the portion of the shock propagating freely because of the absence of such persistent driver may only survive close to the Sun but weaken as it propagates into the IP medium. The magnetic connection between each spacecraft and the portions of the shock that are able to accelerate particles as it propagates away from the Sun determines the shape of the SEP intensity-time profiles.

The observation of the shock S by at least *STEREO-B*, *Juno*, *MESSENGER* and L1 observers allows us to delimit the longitudinal extent of the shock as it propagated into IP space: when it arrived at ~ 1 au was 82° westward of the flare site and 78° eastward of the flare site (i.e., $\sim 160^\circ$ wide), and, if we include the *MESSENGER* observation, it was 113° westward of the flare site when it arrived at 0.4 au. Therefore, the maximum extent of the shock in the IP medium was at least 113° westward and 78° eastward of the flare site (i.e., a total width of 191°). If the shock S was also observed by *STEREO-A*, we can extend its longitudinal extent to $\sim 230^\circ$.

The observation of the SEP event at different radial and longitudinal distances (Figure 1) allows us to determine the longitudinal dependence of the peak intensities at the time of the shock passage (Figure 14(d)) and at the prompt component of the event (Figure 14(c)). These dependences are consistent with average dependences obtained over a large sample of

events at $R \lesssim 1$ au (e.g., Lario et al. 2006, 2013; Richardson et al. 2014).

At the estimated release times of the particles, the portion of the shock front connected to each spacecraft was already at relatively high altitudes ($\gtrsim 2 R_{\odot}$) over the solar surface (Table 3). At this time the shock fitted using coronagraph images was mostly quasi-perpendicular at the cobpoint of *STEREO-A* and more quasi-parallel at the cobpoint of *STEREO-B*, but both spacecraft detected Fe-rich intensities. The release of particles observed at L1 is estimated to occur later in time, when the fitted shock had already expanded to high altitudes, without leaving any signature in the EUV images at the supposed connection location of the L1 spacecraft. Nonetheless, the SEP event at L1 was also Fe-rich at high energies which challenges the scenarios proposed to explain elemental abundances in SEP events (e.g., Cohen et al. 2013, and references therein).

The more gradual SEP intensity increase observed at L1 with respect to the two *STEREO* spacecraft responds to the motion of the cobpoint along the shock front as the shock propagates in IP space (Heras et al. 1995). The more gradual increase observed at L1 for low-energy protons (bottom panel of Figure 1(c)) and low-energy ions (Figure 8(c)) with respect to the faster increase observed for electrons (Figure 8(a)) and high-energy ions and protons (Figures 8(a) and (c)) may be due to a rigidity-dependent transport for the particles to escape from the shock front. Similar differences in low and high energy ion intensities were observed for the event on 2005 January 20 (e.g., Figure 2 in Mason et al. 2012).

We acknowledge the *STEREO* PLASTIC, IMPACT, SECCHI, SWAVES; *SOHO* LASCO, EIT, ERNE, EPHIN; *ACE* EPAM, MAG, SWEPAM; *Wind* 3DP, MFI, WAVES; *MESSENGER* EPS, MAG; *Juno* JEDI, MAG and *SDO* AIA, HMI teams for providing the data used in this paper. The *SDO/AIA* and *SDO/HMI* data are provided by the Joint Science Operations Center (JSOC) Science Data Processing (SDP). *SDO* is the first mission to be launched for NASA's Living With a Star (LWS) Program. The *STEREO/SECCHI* data are produced by an international consortium of the NRL (USA), LMSAL (USA), NASA-GSFC (USA), RAL (UK), University of Birmingham (UK), MPS (Germany), CSL (Belgium), IOTA (France), and IAS (France). *SOHO* is a mission of international cooperation between ESA and NASA. The *ACE* data are provided by the *ACE* Science Center and the *Wind* data by the Coordinated Data Analysis Web. The present work benefited from discussions held at the International Space Science Institute (ISSI, Bern, Switzerland) within the frame of the international teams "Exploration of the inner Heliosphere what we have learned from Helios and what we want to study with Solar Orbiter," led by Dr. W. Droege, and "The Connection Between Coronal Shock Wave Dynamics and Early SEP Production," led by Dr. K. Kozarev and Dr. N. Nitta. D.L. acknowledges the support from NASA under grants NNX11A083G, NNX15AD03G and the *ACE* grant NNX10AT75G. R.Y.K. acknowledges the support from NASA grant NNX13AV35I. RGH acknowledges the financial support by the Spanish MINECO under project AYA2012-39810-C02-01 and ESP2013-48346-C2-1-R. N.D. acknowledges the *STEREO/SEPT* Chandra/EPHIN and *SOHO/EPHIN* project which is supported under grant 50OC1302 by the Federal Ministry of Economics and Technology on the basis of a decision by the German Bundestag. We thank the reviewer for

his/her comprehensive reports. We acknowledge Janvier Wijaya (PredSci) for providing MAS model results, J.E.P. Connerney (NASA/GSFC) for providing *Juno* magnetic field data, and W. S. Kurth (University of Iowa) for discussions on the shock observations at *Juno*.

REFERENCES

- Abraham-Shrauner, B., & Yun, S. H. 1976, *JGR*, **81**, 2097
- Acuña, M. H., Curtis, D., Scheifele, J. L., et al. 2008, *SSRv*, **136**, 203
- Anderson, B. J., Acuña, M. H., Lohr, D. A., et al. 2007, *SSRv*, **131**, 417
- Andrews, G. B., Zurbuchen, T. H., Mauk, B. H., et al. 2007, *SSRv*, **131**, 523
- Bagenal, F., Adriani, A., Allegrini, F., et al. 2014, *SSRv*, in press
- Bothmer, V., Posner, A., Kunow, H., et al. 1997, in *Correlated Phenomena at the Sun, in the Heliosphere and in Geospace*, ed. A. Wilson (ESA SP-415; Noordwijk: ESA), 207
- Bougeret, J. L., Goetz, K., Kaiser, M. L., et al. 2008, *SSRv*, **136**, 487
- Bougeret, J. L., Kaiser, M. L., Kellogg, P. J., et al. 1995, *SSRv*, **71**, 231
- Brueckner, G. E., Howard, R. A., Koomen, M. J., et al. 1995, *SoPh*, **162**, 357
- Cane, H. V. 1996, in *AIP Conf. Ser. 374 High-Energy Solar Physics*, ed. R. Ramaty, N. Mandzhavidze, & X.-M. Hus (Melville, NY: AIP), 124
- Cane, H. V., McGuire, R. E., & von Roseninge, T. T. 1986, *ApJ*, **301**, 448
- Cane, H. V., Reames, D. V., & von Roseninge, T. T. 1988, *JGR*, **93**, 9555
- Cliver, E. W., Kahler, S. W., Neidig, D. F., et al. 1995, *ICRC*, **4**, 257
- Cliver, E. W., Thompson, B. J., Lawrence, G. R., et al. 2005, *ICRC*, **1**, 121
- Cohen, C. M. S., Mason, G. M., Mewaldt, R. A., & von Roseninge, T. T. 2013, in *AIP Conf. Ser. 1539, Solar Wind 13: Proc. Thirteenth Int. Solar Wind Conf.*, ed. G. P. Zank (Melville, NY: AIP), 151
- Connerney, J. E., Oliverson, R. J., Espley, J. R., et al. 2013, in *AGU Fall Meeting Abstracts*, SM21E-04
- Desai, M. I., Mason, G. M., Gold, R. E., et al. 2006, *ApJ*, **649**, 470
- Dodson, H. W., & Hedeman, E. R. 1969, *SoPh*, **9**, 278
- Dresing, N., Gómez-Herrero, R., Heber, B., et al. 2014, *A&A*, **567**, A27
- Dresing, N., Gómez-Herrero, R., Klassen, A., et al. 2012, *SoPh*, **281**, 281
- Dröge, W., Kartavykh, Y. Y., Dresing, N., Heber, B., & Klassen, A. 2014, *JGRA*, **119**, 6074
- Galvin, A. B., Kistler, L. M., Popecki, M. A., et al. 2008, *SSRv*, **136**, 437
- Giacalone, J. 2012, *ApJ*, **761**, 28
- Gold, R. E., Krimigis, S. M., Hawkins, S. E., III, et al. 1998, *SSRv*, **86**, 541
- Gómez-Herrero, R., Dresing, N., Klassen, A., et al. 2015, *ApJ*, **799**, 55
- Gopalswamy, N., Mäkelä, P., Yashiro, S., et al. 2015, *JPhCS*, **642**, 012012
- Heras, A. M., Sanahuja, B., Lario, D., et al. 1995, *ApJ*, **445**, 497
- Heras, A. M., Sanahuja, B., Sanderson, T. R., Marsden, R. G., & Wenzel, K.-P. 1994, *JGR*, **99**, 43
- Howard, R. A., Moses, J. D., Vourlidas, A., et al. 2008, *SSRv*, **136**, 67
- Huttunen-Heikinmaa, K., Valtonen, E., & Laitinen, T. 2005, *A&A*, **442**, 673
- Jian, L., Russell, C. T., Luhmann, J. G., & Skoug, R. M. 2006, *SoPh*, **239**, 393
- Jian, L. K., Russell, C. T., Luhmann, J. G., Galvin, A. B., & Simunac, K. D. C. 2013, in *AIP Conf. Ser. 1539, Thirteenth International Solar Wind Conference*, ed. G. P. Zank (Melville, NY: AIP), 191
- Kallenrode, M.-B., Cliver, E. W., & Wibberenz, G. 1992, *ApJ*, **391**, 370
- Krucker, S., & Hudson, H. 2014, http://sprg.ssl.berkeley.edu/tohban/wiki/index.php/A_Wonderful_Cycle_24_Flare
- Krucker, S., Larson, D. E., Lin, R. P., & Thompson, B. J. 1999, *ApJ*, **519**, 864
- Kwon, R.-Y., Ofman, L., Olmedo, O., et al. 2013, *ApJ*, **766**, 55
- Kwon, R.-Y., Zhang, J., & Olmedo, O. 2014, *ApJ*, **794**, 148
- Kwon, R.-Y., Zhang, J., & Vourlidas, A. 2015, *ApJL*, **799**, L29
- Laitinen, T., Huttunen-Heikinmaa, K., Valtonen, E., & Dalla, S. 2015a, *ApJ*, **806**, 114
- Laitinen, T., Kopp, A., Effenberger, F., Dalla, S., & Marsh, M. S. 2015b, arXiv:1508.03164
- Lario, D., Aran, A., Agueda, N., & Sanahuja, B. 2007, *AdSpR*, **40**, 289
- Lario, D., Aran, A., Gómez-Herrero, R., et al. 2013, *ApJ*, **767**, 41
- Lario, D., Hu, Q., Ho, G. C., et al. 2005, in *Solar Wind 11/SOHO 16, Connecting Sun and Heliosphere*, ed. B. Fleck, T. H. Zurbuchen, & H. Lacoste (ESA SP-592; Noordwijk: ESA), 81
- Lario, D., Kallenrode, M.-B., Decker, R. B., et al. 2006, *ApJ*, **653**, 1531
- Lario, D., Marsden, R. G., Sanderson, T. R., et al. 2000, *JGR*, **105**, 18251
- Lario, D., Raouafi, N. E., Kwon, R.-Y., et al. 2014, *ApJ*, **797**, 8
- Lario, D., Roelof, E. C., Decker, R. B., & Reisenfeld, D. B. 2003, *AdSpR*, **32**, 579
- Lario, D., & Simnett, G. M. 2004, *GMS*, **141**, 195
- Lemen, J. R., Title, A. M., Akin, D. J., et al. 2012, *SoPh*, **275**, 17
- Lin, R. P., Anderson, K. A., Ashford, S., et al. 1995, *SSRv*, **71**, 125
- Long, D. M., Baker, D., Williams, D. R., et al. 2015, *ApJ*, **799**, 224

- Luhmann, J. G., Curtis, D. W., Schroeder, P., et al. 2008, *SSRv*, **136**, 117
- Mason, G. M., Gold, R. E., Krimigis, S. M., et al. 1998, *SSRv*, **86**, 409
- Mason, G. M., Korth, A., Walpole, P. H., et al. 2008, *SSRv*, **136**, 257
- Mason, G. M., Li, G., Cohen, C. M. S., et al. 2012, *ApJ*, **761**, 104
- Mauk, B. H., Haggerty, D. K., Jaskulek, S. E., et al. 2013, *SSRv*, in press
- McComas, D. J., Bame, S. J., Barker, P., et al. 1998, *SSRv*, **86**, 563
- McGuire, R. E., Lal, N., & Van Hollebeke, M. A. I. 1983, *ICRC*, **10**, 353
- McKibben, R. B. 1972, *JGR*, **77**, 3957
- McKibben, R. B., Connell, J. J., Lopate, C., et al. 2003, *AnGeo*, **21**, 1217
- Mewaldt, R. A., Cohen, C. M. S., Cook, W. R., et al. 2008, *SSRv*, **136**, 285
- Miteva, R., Klein, K.-L., Kienreich, I., et al. 2014, *SoPh*, **289**, 2601
- Müller-Mellin, R., Böttcher, S., Falenski, J., et al. 2008, *SSRv*, **136**, 363
- Müller-Mellin, R., Kunow, H., Fleißner, V., et al. 1995, *SoPh*, **162**, 483
- Papaioannou, A., Malandraki, O. E., Dresing, N., et al. 2014, *A&A*, **569**, A96
- Park, J., Innes, D. E., Bucik, R., & Moon, Y.-J. 2013, *ApJ*, **779**, 184
- Park, J., Innes, D. E., Bucik, R., Moon, Y.-J., & Kahler, S. W. 2015, *ApJ*, **808**, 3
- Patsourakos, S., & Vourlidas, A. 2009, *ApJL*, **700**, L182
- Pesnell, W. D., Thompson, B. J., & Chamberlin, P. C. 2012, *SoPh*, **275**, 3
- Posner, A., Bothmer, V., Kunow, H., et al. 1997, in *Correlated Phenomena at the Sun, in the Heliosphere and in Geospace*, ed. A. Wilson (ESA SP-415; Noordwijk: ESA), 377
- Prise, A. J., Harra, L. K., Matthews, S. A., Long, D. M., & Aylward, A. D. 2014, *SoPh*, **289**, 1731
- Reames, D. V. 1995, *AdSpR*, **15**, 41
- Reames, D. V., Barbier, L. M., & Ng, C. K. 1996, *ApJ*, **466**, 473
- Richardson, I. G., & Cane, H. V. 1993, *JGR*, **98**, 15295
- Richardson, I. G., von Rosenvinge, T. T., Cane, H. V., et al. 2014, *SoPh*, **289**, 3059
- Riley, P., Linker, J. A., Lionello, R., & Mikic, Z. 2012, *JASTP*, **83**, 1
- Rouillard, A. P., Sheeley, N. R., Tylka, A., et al. 2012, *ApJ*, **752**, 44
- Sarris, E. T., & Krimigis, S. M. 1985, *SoPh*, **96**, 413
- Schatten, K. H., Wilcox, J. M., & Ness, N. F. 1969, *SoPh*, **6**, 442
- Scherrer, P. H., Schou, J., Bush, R. I., et al. 2012, *SoPh*, **275**, 207
- Smart, D. F., & Shea, M. A. 1985, *JGR*, **90**, 183
- Smith, C. W., L'Heureux, J., Ness, N. F., et al. 1998, *SSRv*, **86**, 613
- Smith, Z., & Dryer, M. 1990, *SoPh*, **129**, 387
- Solomon, S. C., McNutt, R. L., Gold, R. E., & Domingue, D. L. 2007, *SSRv*, **131**, 3
- Stone, E. C., Cohen, C. M. S., Cook, W. R., et al. 1998, *SSRv*, **86**, 357
- Strauss, R. D., & Fichtner, H. 2015, *ApJ*, **801**, 29
- Torsti, J., Kocharov, L., Teittinen, M., et al. 1999a, *JGR*, **104**, 9903
- Torsti, J., Kocharov, L. G., Teittinen, M., & Thompson, B. J. 1999b, *ApJ*, **510**, 460
- Torsti, J., Valtonen, E., Lumme, M., et al. 1995, *SoPh*, **162**, 505
- Tylka, A. J., Cohen, C. M. S., Dietrich, W. F., et al. 2005, *ApJ*, **625**, 474
- Vainio, R., Valtonen, E., Heber, B., et al. 2013, *JSWSC*, **3**, A260000
- Veronig, A. M., Temmer, M., Vršnak, B., & Thalmann, J. K. 2006, *ApJ*, **647**, 1466
- von Rosenvinge, T. T., Reames, D. V., Baker, R., et al. 2008, *SSRv*, **136**, 391
- Vourlidas, A., Lynch, B. J., Howard, R. A., & Li, Y. 2013, *SoPh*, **284**, 179
- Wang, L. 2009, PhD thesis, Univ. California
- Wibberenz, G., & Cane, H. V. 2006, *ApJ*, **650**, 1199
- Wiedenbeck, M. E., Mason, G. M., Cohen, C. M. S., et al. 2013, *ApJ*, **762**, 54
- Wills-Davey, M. J., & Thompson, B. J. 1999, *SoPh*, **190**, 467
- Winslow, R. M., Anderson, B. J., Johnson, C. L., et al. 2013, *JGRA*, **118**, 2213
- Wuelser, J.-P., Lemen, J. R., Tarbell, T. D., et al. 2004, *Proc. SPIE*, **5171**, 111
- Zank, G. P., Li, G., Florinski, V., et al. 2006, *JGRA*, **111**, A06108
- Zhang, M., Qin, G., & Rassoul, H. 2009, *ApJ*, **692**, 109